Characterizing and Tailoring Spatial Correlations in Multimode Parametric Down-Conversion

Vatshal Srivastav,* Natalia Herrera Valencia, Saroch Leedumrongwatthanakun, Will McCutcheon, and Mehul Malik†

Institute of Photonics and Quantum Sciences (IPAQS), Heriot-Watt University, Edinburgh, United Kingdom

(Received 14 October 2021; revised 11 May 2022; accepted 6 September 2022; published 2 November 2022)

Photons entangled in their position-momentum degrees of freedom serve as an elegant manifestation of the Einstein-Podolsky-Rosen paradox, while also enhancing quantum technologies for communication, imaging, and computation. The multimode nature of photons generated in parametric down-conversion has inspired a generation of experiments on high-dimensional entanglement, ranging from complete quantum state teleportation to exotic multipartite entanglement. However, precise characterization of the underlying position-momentum state is notoriously difficult due to limitations in detector technology, resulting in a slow and inaccurate reconstruction riddled with noise. Furthermore, theoretical models for the generated two-photon state often forgo the importance of the measurement system, resulting in a discrepancy between theory and experiment. Here we formalize a description of the two-photon wave function in the spatial domain, referred to as the collected joint-transverse momentum amplitude (JTMA), which incorporates both the generation and measurement system involved. We go on to propose and demonstrate a practical and efficient method to accurately reconstruct the collected JTMA using a simple phase-step scan known as the $2D\pi$ measurement. Finally, we discuss how precise knowledge of the collected JTMA enables us to generate tailored high-dimensional entangled states that maximize discrete-variable entanglement measures such as entanglement of formation or entanglement dimensionality, and optimize critical experimental parameters such as photon heralding efficiency. By accurately and efficiently characterizing photonic position-momentum entanglement, our results unlock its full potential for discrete-variable quantum information science and lay the groundwork for future quantum technologies based on multimode entanglement.

DOI: 10.1103/PhysRevApplied.18.054006

I. INTRODUCTION

The Einstein, Podolsky, and Rosen (EPR) paradox lies at the heart of quantum mechanics [1]. Using the paradigmatic example of two quantum particles sharing perfect correlations (or anticorrelations) between their complementary properties of position and momentum, EPR postulated an inconsistency between local realism and the completeness of quantum mechanics [2]. A physical realization of the original EPR experiment proved challenging, and much of the subsequent theoretical and experimental work focused on a discrete version of the EPR paradox postulated by Bohm and formalized by Bell's inequality [3–5]. While discrete-variable experiments such as ones based on polarization [6,7] have laid the foundation for the quantum technologies of today, the exploration of continuous quantum properties in the vein of the original EPR gedankenexperiment has recently flourished [8–13], thanks to a series of experimental advances and several practical motivations.

Pairs of photons produced in nonlinear spontaneous parametric down-conversion (SPDC) provide a natural platform for tests of EPR entanglement. Photons generated in SPDC are correlated or anticorrelated in their position and momentum owing to the conservation of energy and momentum that governs this process [14–19]. While this source was adapted for the earliest violations of Bell's inequality based on discrete-variable polarization entanglement, the ability to harness its inherent position-momentum correlations has led to a recent explosion of interest in high-dimensional entanglement of photonic spatial modes [20–22]—ranging from demonstrations of high-dimensional Bell-like inequalities and witnesses [23–26], composite quantum state teleportation [27], to exotic forms of multiphoton entanglement [28–31]. High-dimensional (qudit) entanglement also provides significant advantages

*vs54@hw.ac.uk
†m.malik@hw.ac.uk

over qubit-based systems in the form of increased information capacity [32–37] and robustness to noise [38–42], making it a very promising platform for next-generation quantum technologies such as device-independent quantum cryptography [43]. Thus, the ability to efficiently and accurately characterize the underlying two-photon state entangled in its continuous position-momentum degrees of freedom is of paramount importance.

Modeling the generation of entangled photons in a continuum of modes allows for the identification of the effective number of entangled modes that are present in the system [17,44]—the so-called *generation bandwidth*. In addition, precise knowledge of the continuous position-momentum correlations is crucial for accurately tailoring spatial mode bases that maximize metrics relevant to discrete-variable quantum information processing, such as the entanglement of formation (E_{oF}), entanglement dimensionality, and the state fidelity. Experimental reconstruction of a position-momentum entangled state presents some unique challenges—detector technology limits one to scanning through the position and momentum space of interest with a single-mode detector, which inherently introduces loss and involves very long measurement times [45,46]. Recent work has pushed the capabilities of arrayed single-photon detectors to reconstruct such states faster [11–13,47]; however, these techniques still suffer from resolution limits, loss, and an associated large background noise.

In this work, we formulate a theoretical model for the two-photon position-momentum entangled state described by its collected joint-transverse momentum amplitude (JTMA). We show that the collected JTMA is characterized by specific parameters that depend on the state generation as well as the measurement system used in an experiment. We propose and demonstrate a practical and fast method to measure these parameters using a simple π-phase step scan, akin to a classical knife-edge measurement of a laser beam. Our method, referred as the $2D\pi$ measurement, allows us to characterize the collected JTMA without prior knowledge of the optical system and crystal properties. While here we implement our measurement technique with programmable phase-only spatial light modulators, its simplicity enables it to be performed with low-cost components such as a microscope glass slide. We demonstrate the versatility of our measurement scheme by implementing it on two experiments in the continuous-wave near-infrared and pulsed telecom wavelength regimes. Finally, we discuss how accurate knowledge of the collected JTMA enables us to generate tailored discrete-variable high-dimensional entangled states that maximize a desired property such as entanglement of formation or entanglement dimensionality, or optimize experimental measures such as photon heralding efficiency. Our methods have significant potential implications for entanglement-based quantum technologies as well as fundamental tests of quantum mechanics, and can be translated to other continuous degrees of freedom such as time frequency in a straightforward manner.

II. THEORY

A. Collected biphoton JTMA

As shown in Fig. 1(a), the process of SPDC results in the generation of a two-photon state whose correlations in momentum space can be well approximated by a function that we call the *joint-transverse momentum amplitude*. In Appendix A, we derive the full JTMA of the two-photon wave function produced in pulsed, type-II SPDC by a periodically poled nonlinear crystal designed to achieve phase matching at degenerate frequencies in the collinear configuration. At degenerate frequencies and imposing a Gaussian transverse pump profile across the crystal, we show how it approximates the well-known form [17,44]

$$F(\mathbf{q}_s, \mathbf{q}_i) = \mathcal{N}_1 \underbrace{\exp\left(\frac{-|\mathbf{q}_s + \mathbf{q}_i|^2}{2\sigma_P^2}\right)}_{\text{pump profile}} \times \underbrace{\text{sinc}\left(\frac{|\mathbf{q}_s - \mathbf{q}_i|^2}{\sigma_S^2}\right)}_{\text{phase-matching condition}}, \tag{1}$$

where $\mathbf{q}_s$ ($\mathbf{q}_i$) is the transverse-momentum wave vector for the signal (idler) photon and $\mathcal{N}_1$ is a normalization constant. The first term in Eq. (1) incorporates the transverse wave-vector components of the pump, while the second term involves the phase-matching condition imposed on the down-conversion process by the nonlinear crystal. The pump width parameter σ_P depends on the $1/e^2$ beam radius w_p of the pump's intensity profile at the crystal plane, while the generation width parameter σ_S is determined by the crystal length L_z and pump wave vector inside the crystal k_p. These parameters are defined as [48]

$$\sigma_P = \frac{\sqrt{2}}{w_p}, \qquad \sigma_S = \sqrt{\frac{4k_p}{L_z}}. \tag{2}$$

The pump wave vector $k_p = n_P 2\pi/\lambda_P$, where n_P is the refractive index of the nonlinear crystal at pump wavelength λ_P. The interplay between the parameters σ_P and σ_S determines the momentum correlations between the signal and idler photons. In the case where $\sigma_P < \sigma_S$, the parameter σ_P dictates the strength of the momentum correlations, whilst σ_S represents the generation width of the JTMA function [see Fig. 1(b)]. For instance, a very broad (plane-wave) pump beam has $\sigma_P \ll \sigma_S$, and the approximation $\sigma_P \to 0$ can be made. Here, the pump contribution to the JTMA approximates to $\delta(\mathbf{q}_s + \mathbf{q}_i)$, which results in perfect anticorrelations between the signal and idler transverse momenta. In contrast, for a nonzero σ_P, the degree of correlations decreases as σ_P increases. For very thin crystals

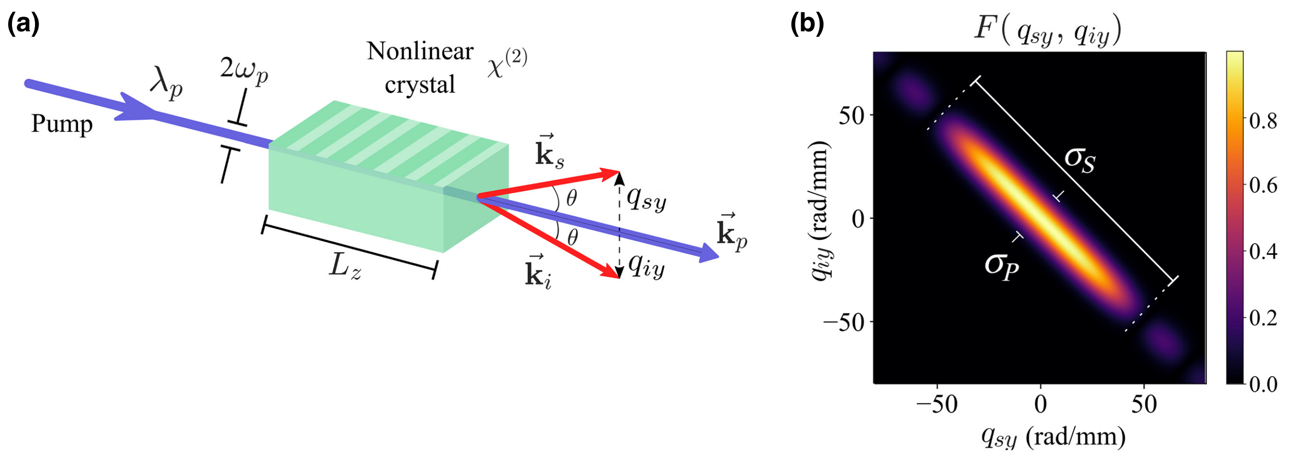

FIG. 1. (a) Spontaneous parametric down-conversion (SPDC): a nonlinear process where a coherent pump photon at wavelength λ_P interacts with a nonlinear crystal ($\chi^{(2)}$) and generates two daughter photons (signal and idler) entangled in their position-momentum degrees of freedom. (b) Joint-transverse momentum amplitude (JTMA): the density plot of a two-dimensional (2D) slice of the JTMA [$F(q_{sx}=0, q_{sy}, q_{ix}=0, q_{iy})$]. The JTMA represents the transverse-momentum correlations between signal and idler photons and is characterized by two parameters, σ_P and σ_S [see Eq. (2)]. The pump bandwidth parameter σ_P is inversely propositional to the beam waist of the pump at the crystal plane (w_P) and dictates the strength of the correlations, while the generation bandwidth parameter σ_S is determined by the length of the crystal L_z and the wavelength of the pump λ_P, and determines the modal generation bandwidth of the JTMA.

($L_z \to 0$), the generation width of the momentum correlation tends to infinity ($\sigma_S \to \infty$). However, as shown in Ref. [49], this approximation breaks for small beam waist w_p, revealing the importance of a finite value of σ_S and σ_P in reality.

Thus far, we have only discussed the generated two-photon state, which solely depends on the pump and crystal parameters σ_P and σ_S. However, the measured momentum correlations also depend on the configuration of the detection system. Photonic spatial modes are routinely measured in the laboratory via a combination of a holographic spatial light modulator (SLM) and single-mode fiber (SMF) that together act as a spatial-mode filter [50,51]. To model the effects of such a spatial-mode filter on the JTMA, we first consider the effect of phase-only SLMs placed in the Fourier plane of the nonlinear crystal. By implementing a diffractive hologram, a SLM can be used to apply an arbitrary amplitude and phase function $\Phi^{(x)}(x)$ on an incident light field, which is then projected onto the Gaussian single mode of the collection fiber. Collection modes have been considered in the context of spatial-mode entanglement [44]. For convenience, we choose to work in momentum space at the crystal plane, so the collection mode takes the form $\mathcal{C}(\mathbf{q}|\sigma_C) = (\sqrt{\pi}\sigma_C)^{-1/2}\exp\{-|\mathbf{q}|^2/\sigma_C^2\}$, characterized by a collection bandwidth σ_C in transverse angular momentum units. However, since the collection mode commutes with the SLM holograms, here we incorporate it into the state itself. We can then model all the properties of the state that we can access and manipulate with SLM holograms by considering the *collected* biphoton JTMA:

$$
\begin{aligned}
G(\mathbf{q}_s, \mathbf{q}_i) &= \mathcal{C}(\mathbf{q}_s|\sigma_C) \times \mathcal{C}(\mathbf{q}_i|\sigma_C) \times F(\mathbf{q}_s, \mathbf{q}_i) \\
&= \frac{\mathcal{N}_1}{\sqrt{\pi}\sigma_C} \underbrace{\exp\left(-\frac{|\mathbf{q}_s|^2}{\sigma_C^2}\right)\exp\left(-\frac{|\mathbf{q}_i|^2}{\sigma_C^2}\right)}_{\text{collection widths}} \\
&\quad \times \underbrace{\exp\left(\frac{-|\mathbf{q}_s+\mathbf{q}_i|^2}{2\sigma_P^2}\right)}_{\text{correlation strength}} \underbrace{\operatorname{sinc}\left(\frac{|\mathbf{q}_s-\mathbf{q}_i|^2}{\sigma_S^2}\right)}_{\text{generation width}}.
\end{aligned} \tag{3}
$$

The choice of σ_C (relative to σ_S and σ_P) limits the entanglement dimension and collection efficiency that can be achieved. In practice, σ_C can be carefully set through a choice of the optical system parameters (discussed in detail in Sec. II B). As can be seen in Fig. 2(a), the effect of including Gaussian collection modes with a specific σ_C suppresses the sinc sidelobes of the generated JTMA [Fig. 1(b)]. We can then write the collected two-photon coincidence (joint) probability of detecting the signal and idler photons when displaying the hologram functions Φ_s and Φ_i, respectively, as

$$
\mathbf{Pr}(\Phi_s, \Phi_i) = \left| \int d^2\mathbf{q}_s \int d^2\mathbf{q}_i \Phi_s(\mathbf{q}_s)\Phi_i(\mathbf{q}_i) G(\mathbf{q}_s, \mathbf{q}_i) \right|^2. \tag{4}
$$

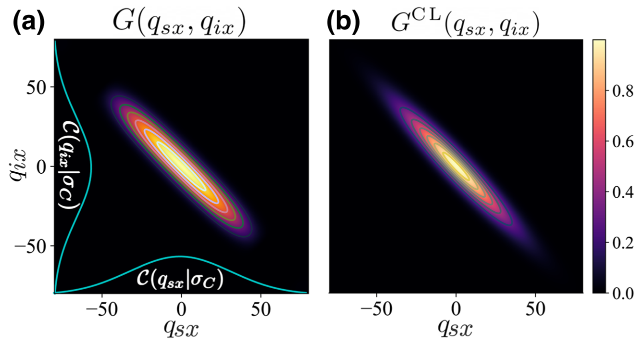

FIG. 2. Collected JTMA. (a) The density plot shows a 2D slice of the collected JTMA $[G(q_{sy} = 0, q_{sx}, q_{iy} = 0, q_{ix})]$ from Eq. (3), where the Gaussian distributions on the axes q_{sx} and q_{ix} represent the collection modes $\mathcal{C}(\mathbf{q}_n|\sigma_C)$ that suppress the sinc sidelobes of the generated JTMA $F(\mathbf{q}_s, \mathbf{q}_i)$ shown in Fig. 1(b). (b) Collected JTMA under the *collection-limited* (CL) approximation, which is valid if $\sigma_S \gtrapprox \sqrt{2}\sigma_C$, resulting in the double-Gaussian form shown in Eq. (8).

B. The 2$D\pi$ measurement

To characterize the collected JTMA of a two-photon state, one requires knowing the parameters σ_P, σ_S, and σ_C. While these parameters can be calculated from the optical system properties, one would practically need to be able to measure them independently and verify that an experimentally generated state is indeed close to what theory predicts. Additionally, this capability is of particular relevance when the optical system is complex, unknown, or inaccessible.

Here, we introduce a simple measurement scheme that we call the 2$D\pi$ measurement, which allows us to estimate the parameters σ_P and σ_C, as well as the center of the state (the axis origins, $\mathbf{q} = 0$) and obtain an accurate two-photon JTMA. This measurement is related to the classical knife-edge measurement routinely used to measure the transverse profile of a laser beam [52]. The 2$D\pi$ measurement can be thought of as a two-photon phase-only knife edge, where a π-phase step is scanned across both the signal and the idler photons, resulting in a 2D function containing information about the two-photon JTMA. The π-phase step is easily implemented via phase-only SLMs placed in each path. The choice of using a phase edge over amplitude edge or slit prevents high photon loss during the measurement, making the 2$D\pi$ measurement an efficient alternative to knife-edge or postselection slit-based experiments [45,53–58]. Here, we assume the apparent rotational symmetry of the JTMA in the joint (q_x, q_y) planes, and scan the π-phase discontinuous profiles for both signal and idler SLMs along the x axis.

In particular, as illustrated in Fig. 3(b), the SLMs display

$$\Phi_n(q_{nx}; a_n) = \begin{cases} 1, & q_{nx} < a_n, \\ -1, & q_{nx} > a_n, \end{cases} \tag{5}$$

where $n \in \{s, i\}$ (signal and idler). By applying the hologram functions Φ_s and Φ_i, the two-photon coincidence probability in Eq. (4) can be expanded to

$$\begin{aligned}\Pr(a_s, a_i) = \Bigg| \int dq_{sy} dq_{iy} \Bigg[&\int_{-\infty}^{a_s} dq_{sx} \int_{-\infty}^{a_i} dq_{ix} G(\mathbf{q}_s, \mathbf{q}_i) \\ &+ \int_{a_s}^{\infty} dq_{sx} \int_{a_i}^{\infty} dq_{ix} G(\mathbf{q}_s, \mathbf{q}_i) \\ &- \int_{-\infty}^{a_s} dq_{sx} \int_{a_i}^{\infty} dq_{ix} G(\mathbf{q}_s, \mathbf{q}_i) \\ &- \int_{a_s}^{\infty} dq_{sx} \int_{-\infty}^{a_i} dq_{ix} G(\mathbf{q}_s, \mathbf{q}_i) \Bigg] \Bigg|^2 .\end{aligned} \tag{6}$$

Because of the sinc dependence in Eq. (3), the integrals in Eq. (6) do not have any known closed analytic forms. Under certain approximations of σ_P and σ_S, one can further simplify the expression in Eq. (6) to ease its numerical evaluation and data fitting. For instance, the approximation of a nearly plane-wave pump beam ($\sigma_P \to 0$) simplifies Eq. (6) to an integral that can be solved straightforwardly. However, the finite apertures in any optical system lead to a nonzero uncertainty in the momentum of the pump, thus resulting in an invalid approximation in practice. Here, we discuss a more practical approximation that accounts for the effect of collection optics and is thus justified from an experimental point of view. We assert that, when the generation bandwidth parameter σ_S is sufficiently large compared to the collection bandwidth parameter σ_C (whilst σ_P remains relatively small), we can replace the sinc argument in Eq. (3) with a Gaussian function. Furthermore, this ensures that the spectral correlations are minimized, justifying the approximations in Appendix A, and keeping the resultant biphoton transverse-momentum state close to pure. This relies on a comparison of the Gaussian envelopes determined by σ_C and the sinc envelope determined by σ_S. In particular, transforming to the sum and difference coordinates, $\mathbf{q}_\pm = (\mathbf{q}_s \pm \mathbf{q}_i)/\sqrt{2}$, we have the collected JTMA

$$\begin{aligned} G(\mathbf{q}_+, \mathbf{q}_-) = &\frac{\mathcal{N}_1}{\sqrt{\pi}\sigma_C} \exp\left\{\frac{-|\mathbf{q}_+|^2}{\tilde{\sigma}_P^2}\right\} \exp\left\{\frac{-|\mathbf{q}_-|^2}{\sigma_C^2}\right\} \\ &\times \mathrm{sinc}\left(\frac{-2|\mathbf{q}_-|^2}{\sigma_S^2}\right), \end{aligned} \tag{7}$$

where $\tilde{\sigma}_P = \left(1/\sigma_C^2 + 1/\sigma_P^2\right)^{-1/2}$ and, for σ_P relatively smaller than σ_C, $\tilde{\sigma}_P \approx \sigma_P$. We then approximate the product of the Gaussian envelope (σ_C) and the sinc argument (σ_S) to a Gaussian, which is valid if $\sigma_S \gtrapprox \sqrt{2}\sigma_C$ (see Appendix B). Under this *collection-limited* (CL) approximation, the *collected* biphoton JTMA (G^{CL}) reads

$$G(\mathbf{q}_+, \mathbf{q}_-) \approx G^{\mathrm{CL}}(\mathbf{q}_+, \mathbf{q}_-) = \frac{\mathcal{N}_1}{\sqrt{\pi}\sigma_C} \exp\left\{-\frac{|\mathbf{q}_s + \mathbf{q}_i|^2}{2\tilde{\sigma}_P^2}\right\} \exp\left\{-\frac{|\mathbf{q}_s - \mathbf{q}_i|^2}{2\sigma_C^2}\right\}. \tag{8}$$

Note that instead of σ_S, σ_C now determines the width of the JTMA [see Fig. 2(b)]. Even though we have gotten rid of the sinc dependence in the collection-limited approximation, there is no analytic expression for the $2D\pi$ measurement. Still, we can derive some contributions analytically, from which we can recover σ_P and σ_C. One must first determine the centers of the collected JTMA on the SLMs, which can be achieved by fitting $\Pr(a, -\infty)$ and $\Pr(-\infty, a)$ (Appendix C). Then we can retrieve the function $\Pr(a, -a)$, which is given as

$$\Pr(a, -a) = \left| N - N' \exp\left(-\frac{2a^2}{\sigma_C^2}\right)\right|^2, \tag{9}$$

where N and N' have absorbed all the constants that are independent of a. The expression $\Pr(a, -a)$ provides information about the collection width parameter σ_C. Finally, a function that retrieves σ_P is $\Pr(a, a)$, which is given as

$$\Pr(a, a) = \mathcal{A}\Bigg[\sqrt{2}\sigma_P e^{-2a^2(1/\tilde{\sigma}_P^2 + 1/\sigma_C^2)} - 2\sqrt{\pi}|a|e^{-2a^2/\sigma_C^2} \times \mathrm{erfc}\left(\frac{\sqrt{2}|a|}{\tilde{\sigma}_P}\right) - \frac{\pi\sigma_C}{2\sqrt{2}}\left\{1 - 2\mathrm{erf}\left(\frac{\sqrt{2}|a|}{\sigma_C}\right)\right\}\Bigg]^2, \tag{10}$$

where erfc is the complementary error function. By fitting Eqs. (9) and (10) to the experimental data corresponding to $\Pr(a, -a)$ and $\Pr(a, a)$, we can obtain σ_C and σ_P that describe the collected JTMA, which subsequently characterizes the spatial correlations produced in spontaneous parametric down-conversion. For detailed calculations of $\Pr(a, -a)$ and $\Pr(a, a)$, see Appendix C.

III. EXPERIMENT AND RESULTS

To demonstrate the versatility of the $2D\pi$ measurement, we perform an experimental implementation at two different pump wavelengths (cw 405 nm and femtosecond pulsed 775 nm). The general setup is the same for both wavelengths [see Fig. 3(a)]. A laser is shaped by a telescope ($L1$ and $L2$) to pump a 5-mm-long periodically poled nonlinear periodically poled potassium titanyl phosphate (PPKTP) crystal that generates a pair of down-converted photons (for 405 nm $\rightarrow \lambda_{s1}, \lambda_{i1} = 810$ nm, for 775 nm $\rightarrow \lambda_{s2}, \lambda_{i2} = 1550$ nm) entangled in their transverse position-momentum degrees of freedom via type-II SPDC. After removing the pump with a dichroic mirror, the generated photons are separated with a polarizing beam splitter and made incident onto two phase-only spatial light modulators (SLM_s and SLM_i) placed in the Fourier plane of the crystal via lens $L3$ ($f = 250$ mm). The spatial field at the SLM plane is directly related to the transverse momentum space at the crystal plane via $\mathbf{q} = 2\pi x/f\lambda$, where f is the focal length of $L3$ and λ is the signal or idler wavelength. We perform the $2D\pi$ measurement using diffractive holograms displayed on the SLMs [Fig. 3(b)], together with the collection of SMFs, allowing for arbitrary spatial-mode projective measurements to be performed on the incoming photons.

The optical system parameters (lenses $L1$–$L5$ and A) are judiciously chosen. First, in order to obtain a highly correlated JTMA, the telescope system of lenses $L1$ and $L2$ is chosen to maximize the pump radius w_P at the crystal plane, thus minimizing the pump width parameter σ_P for the strength of the momentum correlation, while ensuring that the pump beam is not truncated by the crystal aperture. Next, consider the back-propagated beam from the SMF to the PPKTP crystal [shown in red in Fig. 3(c)]. The aspheric lens A and the optical system of lenses $L3$–$L5$ are chosen such that the collection width parameter σ_C meets the condition $\sigma_S \gtrapprox \sqrt{2}\sigma_C$, allowing us to work under the collection-limited JTMA approximation (see the previous section). The telescope system $L4$ and $L5$ has also been referred to in our previous work as an "intensity-flattening telescope" as it effectively broadens the back-propagated Gaussian envelope of the collection mode such that higher-order modes associated with the edges of the JTMA are measured efficiently, while the lower-order modes are suppressed [51].

The photons are detected by single-photon-avalanche photodiodes for $\lambda_{s1}, \lambda_{i1} = 810$ nm and superconducting nanowire detectors for $\lambda_{s2}, \lambda_{i2} = 1550$ nm, which are connected to a coincidence counting logic with a coincidence window of 0.2 ns. We characterize the collected JTMA at the Fourier plane of the crystal located at the SLM planes. The plots in Figs. 4(a) and 4(e) show the data obtained for the $2D\pi$ measurement performed at both wavelengths ($\lambda_{s1}, \lambda_{i1} = 810$ nm and $\lambda_{s2}, \lambda_{i2} = 1550$ nm), while the reconstructed JTMAs are shown in Figs. 4(d) and 4(h). We obtain σ_C and σ_P by fitting the closed-form expressions of $\Pr(a, -a)$ and $\Pr(a, a)$ [Eqs. (9) and (10)] to the experimental data. It is worth noting that the feature corresponding to σ_P is also present in the visibility of $\Pr(a, -a)$, which is shown in the fitting curves in Figs. 4(b) and 4(f) [refer to Eq. (C6)]. Those features, therefore, provide a sensitive measure of the correlation strength σ_P even when the resolution of the scan is coarse, unlike slit-based measurements that present finite slit apertures, thereby suffering from low count rates and resulting in the trade-off between the slit size and photon flux. The $2D\pi$ measurement allows for high count rates as in the measurement of tilting gratings (tilt-basis measurement).

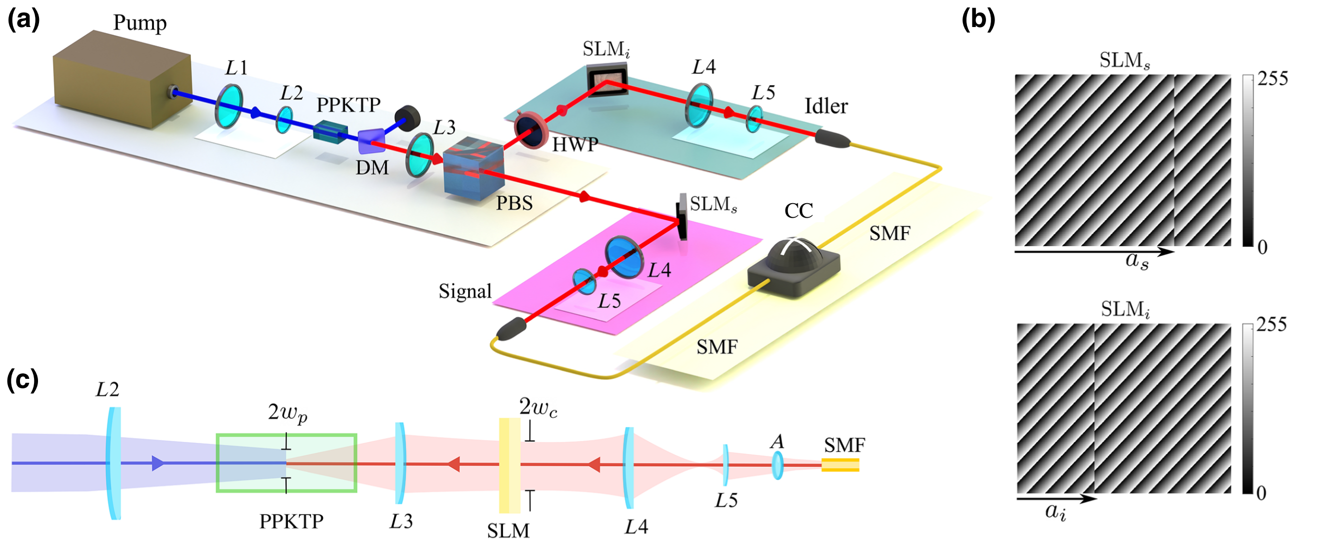

FIG. 3. Experimental setup. (a) A laser is used to pump a nonlinear periodically poled potassium titanyl phosphate (PPKTP) crystal to generate a pair of photons entangled in their transverse position-momentum via type-II SPDC. Our experiment is performed on two parallel setups with a continuous-wave laser diode pump at 405 nm and a pulsed Ti:sapphire pump at 775 nm. The pump photons are filtered by a dichroic mirror (DM) and the down-converted photons are separated with a polarizing beam splitter (PBS). We rotate the polarization of the reflected idler photon from vertical to horizontal using a half-wave-plate (HWP). The signal and idler photons are incident on two phase-only spatial light modulators (SLMs) that are used for performing the $2D\pi$ measurement in the transverse position degree of freedom. The filtered photons are collected by a combination of telescopes ($L4$ and $L5$) and aspheric lenses (A) coupling to single-mode fibers (SMFs), followed by detection through either single-photon-avalanche photodiodes (for $\lambda_{s1}, \lambda_{i1} = 810$ nm) or superconducting nanowire detectors (for $\lambda_{s2}, \lambda_{i2} = 1550$ nm). A coincidence counting (CC) logic is used for recording time-coincident photon detection events within a coincidence window of 0.2 ns. (b) Examples of diffractive computer generated holograms implemented on the signal and idler SLMs for performing the $2D\pi$ measurement in the x direction. (c) Two-dimensional profile of the experimental setup showing the relevant parameters w_P and w_C. The pump beam radius (w_P) at the crystal plane determines the pump width parameter σ_P [Eq. (2)]. The back-propagated collection mode radius (w_C) at the SLM determines the collection width parameter (σ_C) at the crystal, which depends on the single-mode fibers and optical collection system lenses used.

Together, they provide the beam parameters that are crucial for designing accurate projective measurements (Sec. IV) on both SLM and its Fourier planes, i.e. the centers and diameters of the beams, and the strength of quantum correlation.

The measured values of the pump and collection width parameters (σ_P^{meas}, σ_C^{meas}) obtained from the $2D\pi$ measurement are reported in Table I and agree with their predicted values (σ_P^{pre}, σ_C^{pre}), which are calculated from our knowledge of the optical system parameters. The predicted value of the pump width parameter σ_P^{pre} for both wavelengths is calculated from the $1/e^2$ pump radius at the crystal plane [Eq. (2)], and the predicted collection width parameter σ_C^{pre} is calculated by back propagating the width of the fundamental Gaussian mode of the SMFs to the crystal plane [Fig. 3(c)]. The error propagation is analyzed by taking into account ± 0.5 mm uncertainties of the measured distances between lenses and focal lengths.

IV. TAILORING HIGH-DIMENSIONAL ENTANGLEMENT

Once accurate knowledge of the continuous position-momentum two-photon state characterized by the JTMA has been obtained, one may want to discretize such a state for use in quantum information applications based on discrete variables [25,37,59,60]. For instance, to harness discrete variable high-dimensional entanglement, one needs to choose an appropriate modal basis in which to work. The design of such discrete modal bases is often informed by the Schmidt decomposition of the entire biphoton wave function [61,62]. However, at the expense of lower count rates one can design modal bases to optimize for more general figures of merit such as E_{oF}, heralding efficiency, and measurement fidelity, while taking into account the types of devices used (for example, phase-only SLMs).

We begin with a theoretical treatment of how our continuous two-photon state is discretized via specific projective modal measurements. In practice, we display holograms $\{\Phi_s(\mathbf{q}_s)\}^a$ and $\{\Phi_i(\mathbf{q}_i)\}^b$ (where $|\Phi_s(\mathbf{q}_s)| \leq 1$) on the SLMs to generate a subnormalized postselected state $|\psi^{(\text{PS})}\rangle$ in the *standard* discrete modal basis $\{|\hat{e}_n\rangle\}_a$:

$$|\psi^{(\text{PS})}\rangle = \sum_{ab} T_{ab} |\hat{e}_s^a\rangle |\hat{e}_i^b\rangle \tag{11}$$

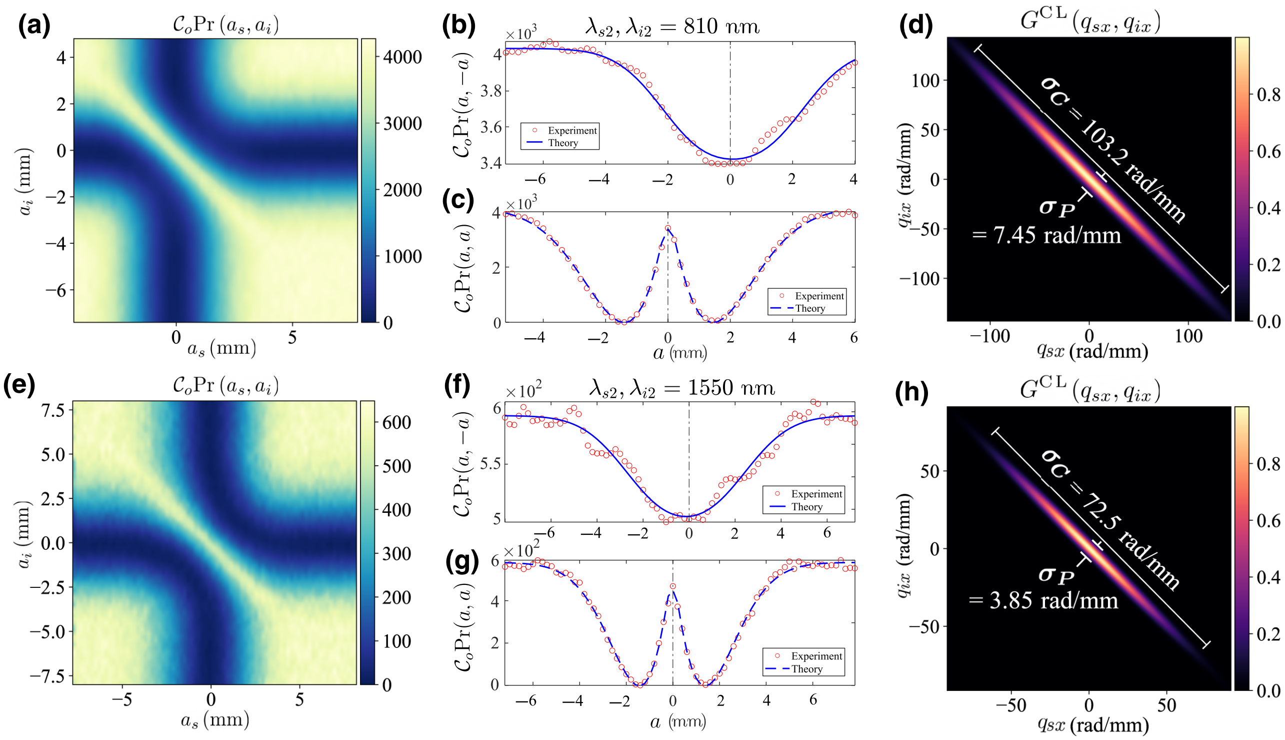

FIG. 4. Experimental results: $2D\pi$ measurement $[\mathcal{C}_o\mathrm{Pr}(a_s, a_i)]$ for (a) $\lambda_{s1}, \lambda_{i1} = 810$ nm and (e) $\lambda_{s2}, \lambda_{i2} = 1550$ nm, where $\mathcal{C}_o$ is proportional to two-photon coincidence count rates. We obtain σ_C and σ_P by fitting $\mathrm{Pr}(a, -a)$ (b),(f) and $\mathrm{Pr}(a, a)$ (c),(g). Panels (d) and (h) show the experimentally determined collected JTMA at both wavelengths, where (d) for $\lambda_{s1}, \lambda_{i1} = 810$ nm, $\sigma_C = 103.2 \pm 1.8$ rad/mm and $\sigma_P = 7.45 \pm 1.51$ rad/mm, and (h) for $\lambda_{s2}, \lambda_{i2} = 1550$ nm, $\sigma_C = 72.5 \pm 2.3$ rad/mm and $\sigma_P = 3.85 \pm 0.31$ rad/mm.

with the complex elements T_{ab} given by

$$T_{ab} = \int d^2\mathbf{q}_s \int d^2\mathbf{q}_i \Phi_s^a(\mathbf{q}_s)\Phi_i^b(\mathbf{q}_i)G(\mathbf{q}_s, \mathbf{q}_i). \tag{12}$$

Here, $G(\mathbf{q}_s, \mathbf{q}_i)$ is the collected JTMA (collection limited in our case) whose form can be obtained via the $2D\pi$ measurement described in the preceding sections. The holograms $\Phi_s^a(\mathbf{q}_s)$ and $\Phi_i^b(\mathbf{q}_i)$ can be constructed in a manner that ensures that the associated discrete modal bases are orthonormal (see Appendix D).

Now we can determine the probabilities associated with measuring generalized projectors (arbitrary coherent superpositions) in both the two-photon and single-photon cases. We can measure an arbitrary normalized vector $|\vec{v}_s\rangle = \sum_a v_s^a |\hat{e}_s^a\rangle$ by constructing hologram $\Phi_s^{\vec{v}}(\mathbf{q}_s)$ given by

$$\Phi_s^{\vec{v}_s}(\mathbf{q}_s) = A^{\vec{v}_s} \sum_a v_s^a \Phi_s^a(\mathbf{q}_s) \tag{13}$$

with $A^{\vec{v}}$ chosen such that $\max_{\mathbf{q}} |\Phi_s^{\vec{v}}(\mathbf{q})| \leq 1$. The preceding condition ensures that a hologram does not increase energy and can only add loss. The two-photon coincidence probability for measuring our state in modes $|\vec{v}_s\rangle$ and $|\vec{v}_i\rangle$ is

TABLE I. Predicted and measured parameters describing the generated and collected JTMA obtained from the $2D\pi$ measurement. The predicted pump width and generation width parameters (σ_P^{pre} and σ_S^{pre}) are obtained from the pump waist w_p and crystal length according to Eq. (2). The predicted collection width parameter (σ_C^{pre}) is calculated from measurements of the optical collection system (see the main text for details). The measured parameters (σ_P^{meas} and σ_C^{meas}) are obtained from the $2D\pi$ measurement performed on the two-photon state. Both predicted and measured values of σ_C meet the condition $\sigma_S \gtrsim \sqrt{2}\sigma_C$ that allows us to operate under the CL approximation [see Eq. (8)].

λ (nm)	w_p (μm)	σ_P^{pre} (rad/mm)	σ_P^{meas} (rad/mm)	σ_S^{pre} (rad/mm)	σ_C^{pre} (rad/mm)	σ_C^{meas} (rad/mm)
810	188 ± 5.3	7.52 ± 0.21	7.45 ± 1.51	151.1 ± 3.1	106.5 ± 12.6	103.2 ± 1.8
1550	450 ± 5.3	3.14 ± 0.04	3.85 ± 0.48	106.7 ± 2.1	76.7 ± 8.01	72.5 ± 2.3

given by

$$\mathbf{Pr}(\vec{v}_s, \vec{v}_i) = (A^{\vec{v}_s} A^{\vec{v}_i})^2 |\langle \vec{v}_s | \langle \vec{v}_i | |\psi^{(\mathrm{PS})}\rangle|^2. \quad (14)$$

Similarly, the probability of measuring a signal photon (inclusive of a possible idler photon) in mode $|\vec{v}_s\rangle$ depends on the collection mode of only the signal $[\mathcal{C}(\mathbf{q}_s|\sigma_C)]$ and is expressed as

$$\mathbf{Pr}(\vec{v}_s) = \int d^2\mathbf{q}_i \left| \int d^2\mathbf{q}_s \Phi_s^{\vec{v}_s}(\mathbf{q}_s)\mathcal{C}(\mathbf{q}_s|\sigma_C)F(\mathbf{q}_s, \mathbf{q}_i) \right|^2, \quad (15)$$

where the product of the generated JTMA $F(\mathbf{q}_s, \mathbf{q}_i)$ and the signal's collection mode $\mathcal{C}(\mathbf{q}_s|\sigma_C)$ can be further simplified as discussed in Appendix B [see Eq. (B4)].

With knowledge of the collected JTMA ($G(\mathbf{q}_s, \mathbf{q}_i)$) and the preceding framework, one can design modal bases [corresponding to holograms $\Phi_s^a(\mathbf{q}_s)$ and $\Phi_i^b(\mathbf{q}_i)$] and choose which measurements to make in a given basis to tailor the state properties freely. Here, we refer closely to the example of disjoint discrete spatial modes (similar to the "pixel basis" [60]) defined by macropixels in the SLM plane to exemplify the design process. In this case for example, the size and shape of each pixel, their positions and the spacing between them, and the size of the complete pixel mask are important parameters to take into account in the basis design. Though, as we will see in a proceeding example, one can tailor these properties for entirely general holograms. Whilst one may freely design holograms that achieve arbitrary states, T_{ab}, count rates, and efficiencies, it is often advantageous to address the following key figures of merit.

Schmidt basis: A standard discrete basis for the postselected two-photon state [Eq. (11)] can be designed such that it corresponds to the Schmidt basis where the coincidence crosstalk between modes is minimized, and thus suppressing the off-diagonal elements of T_{ab} ($T_{ab} \to 0$ for all $a \neq b$). In the case of the pixel basis, this corresponds to choosing the spacing between pixels to be at least equal to the pump width parameter (appropriately propagated to position coordinates at the SLM plane), which determines the JTMA correlation strength $\sigma_P^{(x)} = f\lambda/2\pi\sigma_P$ (see Fig. 5).

Entanglement dimensionality: When constructing a standard discrete basis, there is a limit on the entanglement dimensionality—the maximal number of correlated modes that can be considered whilst remaining in the Schmidt basis. Information about this can be deduced from the JTMA: the accessible number of *generated* entangled modes, related to the reciprocal of the marginal state purity (often known as the Schmidt number [63]), can be estimated through σ_P and σ_S [17]. However, as we have shown here, σ_S is often constrained by the collection width parameter σ_C, knowledge of which can be used to estimate the perhaps more relevant number of *collected* entangled modes. Therefore, the reasonable measure of entangled modes is the *collected* Schmidt number (K_c) defined for $G(\mathbf{q}_s, \mathbf{q}_i)$ [63], and is given as

$$K_c = \frac{1}{4}\left(\frac{\sigma_P}{\sigma_C} + \frac{\sigma_C}{\sigma_P}\right)^2. \quad (16)$$

For the pixel basis, this involves an optimization of the number of correlated macropixels one can fit within the collected area, while having appreciable count rates.

Maximal entanglement: Optimizing the standard discrete basis such that the coincidence probability for each mode is equal (while remaining in the Schmidt basis) imposes the condition that T_{ab} is proportional to the identity matrix and thus a maximally entangled state. This maximizes entropic quantifiers of entanglement such as E_{oF} and can be achieved, for instance, by optimally varying pixel size as a function of radial distance from the optic axis (see Fig. 5 for a detailed example).

Basis-dependent efficiency: One can find bases where all the holograms can be efficiently realized by maximizing $A^{\vec{v}}$ for all elements of a basis. For instance, with disjoint pixels, all bases mutually unbiased to the standard basis obtain $A^{\vec{v}} = \sqrt{d}$ for all elements. This ensures that all measurements maximize photon flux, thus drastically reducing measurement times [60].

Heralding efficiency: The heralding efficiency, or the probability that the detection of a photon in one mode (signal) indicates a photon in the other (the heralded photon or idler), is normally studied in a symmetric configuration, i.e., the same collection parameters apply to both photons [64,65]. The inherent multimode nature of the JTMA opens up an alternate way to tune heralding efficiencies in an asymmetric manner, i.e., with different collection parameters and resultant heralding efficiencies for each photon [66]. We can define a one-sided heralding efficiency in this case, where measuring the signal photon in mode $|\vec{v}_s\rangle$ heralds the presence of an idler photon in mode $|\vec{v}_i\rangle$ with an efficiency

$$\eta^{s\to i} = \frac{\mathbf{Pr}(\vec{v}_s, \vec{v}_i)}{\mathbf{Pr}(\vec{v}_s)}. \quad (17)$$

Therefore, designing holograms $\Phi_i^{\vec{v}}(\mathbf{q}_i)$ to maximize Eq. (17), and choosing bases such that $A^{\vec{v}_i}$ is large can lead to high one-sided heralding efficiency (see Appendix D). For instance, increasing the size of the idler pixel relative to that of the signal optimizes the heralding efficiency, resulting in a larger overlap of heralded photons on the idler side.

We have recently implemented some of the above techniques experimentally in order to rapidly certify high-fidelity entangled states with entanglement dimensionalities up to $d = 55$, entanglement of formation up to

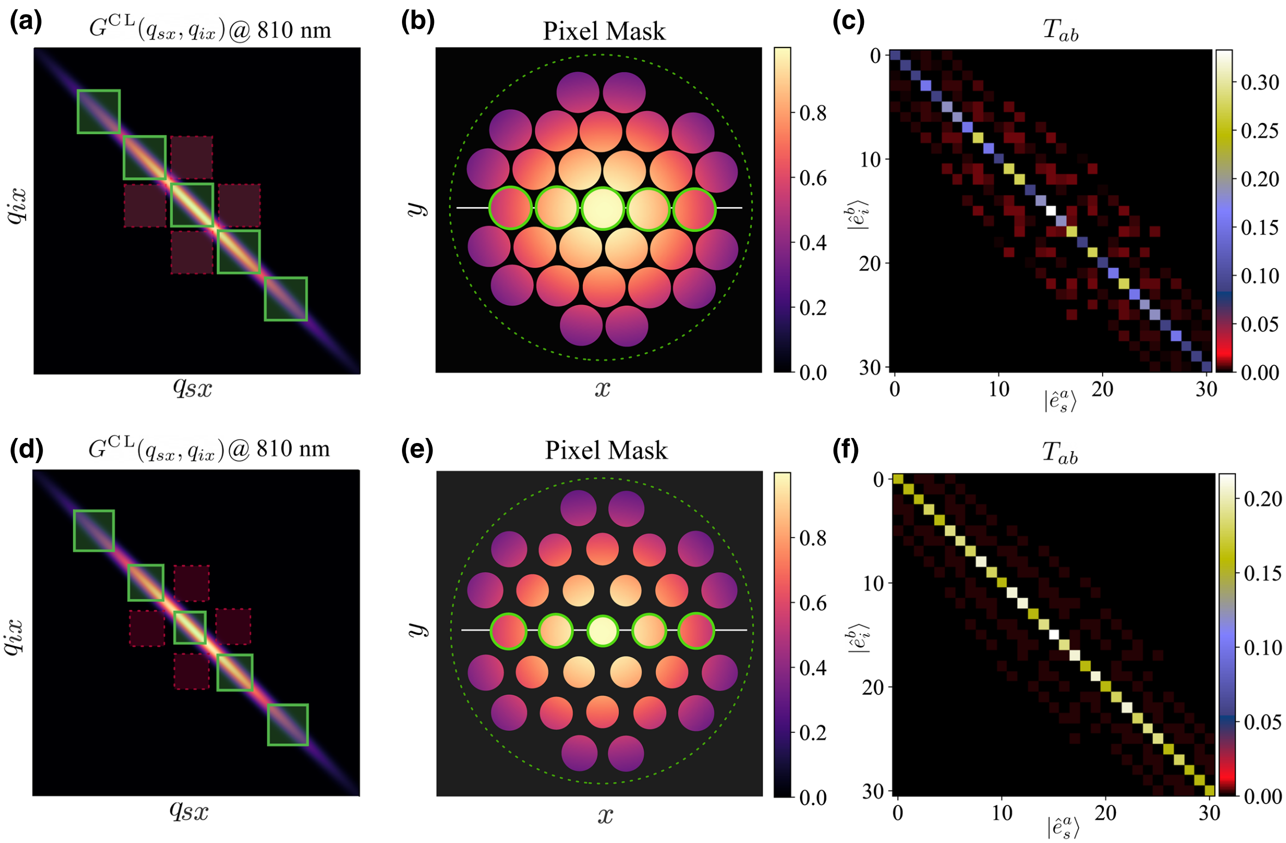

FIG. 5. Optimizing T_{ab} for the 810-nm two-photon state by tailoring the pixel mask in 31 dimensions. Panels (a)–(c) [(d)–(f)] show the collected JTMA, pixel mask holograms, and resulting state coefficients T_{ab} before (after) optimization. The square regions in the JTMA plots in (a) and (d) indicate the values of q_{sx} and q_{ix} used to generate the pixel masks holograms in (b) and (e). The green square regions represent the pixels that are correlated (T_{aa} elements), while the red ones are responsible for crosstalk between them (T_{ab} elements for all $a \neq b$). Note that, while the 2D JTMA (x dimension) is shown here, calculating all the elements of T_{ab} requires integration over the entire 4D expression for the JTMA [Eq. (12)], i.e., q_{sx}, q_{sy}, q_{ix}, and q_{iy}. The green dashed circles represent the maximum size of the detectable areas, which is further constrained by the finite collection bandwidth parameter σ_C. In (a) and (b), the pixels are set to the same size with a fixed spacing between them, and the resulting state (c) shows significant crosstalk between discrete spatial modes. The dimensionality of entanglement (d_{ent}) is calculated to be 26 in the Hilbert space of $d = 31$ pixels [26]. In (d) and (e), we show how one can tailor the pixel mask from knowledge of the JTMA such that the coincidence probability $\Pr(\Phi_s, \Phi_i)$ is equal for all pixels, while minimizing the crosstalk between them at the expense of total counts. This ensures that the state shown in (f) is optimized to be in the Schmidt basis while also being close to maximally entangled. Consequently, the dimensionality of entanglement is increased to its maximal value of $d_{\mathrm{ent}} = 31$.

$E_{\mathrm{oF}} = 4$ ebits [60], and to violate high-dimensional steering inequalities in dimension up to $d = 15$ [67]. These experiments were performed in the pixel basis, where through knowledge of the JTMA obtained via the $2D\pi$ measurement, a postselected state closest to a maximally entangled state was realized. The SLM holograms were designed to minimize the crosstalk between modes, while simultaneously equalizing photon count rates for all discrete modes across σ_C (in a manner similar to the procedure discussed in Fig. 5). Furthermore, high-dimensional entanglement witnesses exploiting only bases mutually unbiased to the standard pixel basis ensured high basis-dependent efficiencies and minimized measurement times.

While the above examples have used the disjoint and discrete pixel basis, knowledge of the JTMA can be used to optimize other spatial mode bases such as the Laguerre-Gaussian (LG) basis, which plays a significant role in classical and quantum optics [20]. In the LG basis, correlations in both the azimuthal and radial components depend on the relationship between the pump and the down-converted signal and idler mode waists [69,70], indicating the effective number of detectable Schmidt modes that are entangled in the full transverse field [48,61]. The ability to

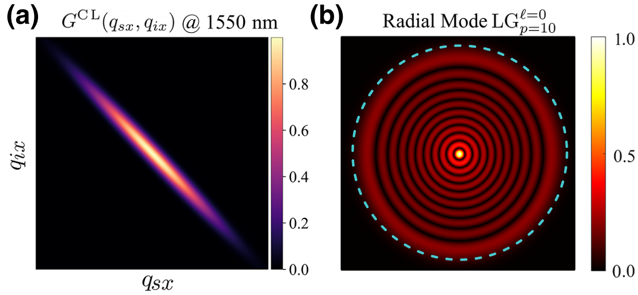

FIG. 6. LG radial-mode entanglement. (a) Knowledge of collected JTMA [$G(\mathbf{q}_s, \mathbf{q}_i)$] determines the maximum size of the mode waist [blue dotted circle in (b)] to witness entanglement in seven dimensions in $p = 0, \ldots, 10$ radial LG modes [68].

determine the collected JTMA allows us to experimentally adjust σ_P and σ_C such that the correlations are maximized. While the degree of correlations relates to σ_P, information of σ_C sets a limit on the size of modes we can optimally measure (see Fig. 6), which is of particular importance when dealing with modes that have radial dependence. Taking these considerations into account, we were able to recently certify entanglement dimensionalities of up to 26 in a 43-dimensional radial and azimuthal LG space [68], demonstrating the potential of the JTMA in harnessing the full capabilities of high-dimensional entanglement.

V. CONCLUSION AND DISCUSSION

In our work, we have studied the spatial wave function of position-momentum entangled biphoton states generated in collinear type-II SPDC. We define the collected JTMA, a function that characterizes the biphoton state in the momentum degree of freedom while incorporating the effects of the measurement system. We propose a method to efficiently and accurately characterize the collected JTMA using phase-only modulated holograms, and experimentally demonstrate it on two identical entanglement sources at different wavelengths. From knowledge of the collected JTMA, we discuss how one can tailor discrete-variable high-dimensional entangled states via projective measurements in several spatial mode bases. Our techniques can be used to generate high-fidelity, high-dimensional entangled states of light, which can be further optimized for properties such as maximal entanglement and single-photon heralding efficiencies. The utility of our characterization methods is evident in some recent works, where we have used knowledge of the JTMA to tailor diverse kinds of high-dimensional entangled states of light with record quality and dimensionalities in device-dependent [60,68] as well as one-sided device-independent platforms [42,67].

Information about the JTMA could be used for implementing and optimizing arbitrary spatial-mode projective measurements and generalized unitaries [51,71], which are required for violating Bell-like inequalities proposed for high-dimensional systems. Additionally, knowledge of the JTMA can be used for tuning one-sided photon heralding efficiencies [42,72–74], which play a significant role in device-independent tests of quantum mechanics and the related field of device-independent quantum key distribution. The ability to control the correlations and anticorrelations of an entangled pair of photons using the measured JTMA parameters could enable the engineering of quantum states with tailored spatial and spectral properties [18], which could be used to boost the performance of quantum-enhanced imaging and metrology [75,76]. In addition, our methods for characterizing the JTMA can be translated to other degrees of freedom such as time frequency [77–79], and could enable the characterization of the full spatiotemporal biphoton wave function, which would have a wide-ranging impact on entangled-based quantum technologies.

ACKNOWLEDGMENTS

This work is supported by the QuantERA ERA-NET Co-fund (FWF Project I3773-N36), the UK Engineering and Physical Sciences Research Council (EPSRC) (EP/P024114/1), and the European Research Council (Starting Grant PIQUaNT).

APPENDIX A: JTMA OF TYPE-II SPDC WITH PERIODIC POLING

We consider the case of type-II SPDC (whereby the pump, signal, and idler are polarized on the e, e, and o axes, respectively) for periodically poled crystals designed to achieve phase matching at degenerate signal and idler frequencies in the collinear configuration. To account for all these contributions, we derive an expression for the entire biphoton state, and apply approximations to arrive at the JTMA stated in the main text [Eq. (1)]. Following the conventional asymptotic fields approach, the first-order nonlinear Hamiltonian in the backward-Heisenberg picture, $H^{\mathrm{NL}}(t)$ (see Ref. [80] for a detailed account) takes the form

$$\int H^{\mathrm{NL}}(t)dt \propto \int dt \int d^3\mathbf{k}_i \int d^3\mathbf{k}_s \int d^3\mathbf{k}_p \times \int d^3\mathbf{x} \exp\left(i(\mathbf{k}_s + \mathbf{k}_i - \mathbf{k}_p)\cdot\mathbf{x}\right)\chi^{(2)}(\mathbf{x}) \times \exp\left(i[\omega(\mathbf{k}_s) + \omega(\mathbf{k}_i) - \omega(\mathbf{k}_p)]t\right)\alpha_p(\mathbf{k}_p)\hat{a}_s^{\dagger}(\mathbf{k}_s) \times \hat{a}_i^{\dagger}(\mathbf{k}_i) + \mathrm{H.c.} \tag{A1}$$

The temporal integral can be extended over all time, leading to the energy-matching term, $\int dt \exp(i\Delta\omega t) = \delta(\Delta\omega) = \delta[\omega(\mathbf{k}_s) + \omega(\mathbf{k}_i) - \omega(\mathbf{k}_p)]$. The $d^3\mathbf{x}$ integral over a crystal of dimensions $L_x^\perp \times L_y^\perp \times L_z$, situated about the origin can be evaluated as

$$\begin{aligned}
&\int_{-L_x^\perp/2}^{L_x^\perp/2} dx_x \int_{-L_y^\perp/2}^{L_y^\perp/2} dx_y \int_{-L_z/2}^{L_z/2} dx_z \exp\left(i(\mathbf{k}_s + \mathbf{k}_i - \mathbf{k}_p)\cdot\mathbf{x}\right)\chi^{(2)}(\mathbf{x}) \\
&= \operatorname{sinc}\left(\frac{L_x^\perp}{2}(q_{sx} + q_{ix} - q_{px})\right)\operatorname{sinc}\left(\frac{L_y^\perp}{2}(q_{sy} + q_{iy} - q_{py})\right)\operatorname{sinc}\left(\frac{L_z}{2}\Delta k_z\right) \\
&\approx \delta(\mathbf{q}_s + \mathbf{q}_i - \mathbf{q}_p)\operatorname{sinc}\left(\frac{L_z}{2}\Delta k_z\right),
\end{aligned} \tag{A2}$$

where we introduce notation $\mathbf{q}_n$ for the transverse components of $\mathbf{k}_n$ (for $n = s, i, p$), and the longitudinal wave-vector mismatch, Δk_z (to be defined), contains a contribution from the periodic poling structure with period Λ. The final approximation will hold for crystals with transverse extents $(L_x^\perp, L_y^\perp)$ that are sufficiently large.

Using the approximations above, the integral in Eq. (A1) can be written as

$$\begin{aligned}
\int H^{\mathrm{NL}}(t)dt \propto \int d^3\mathbf{k}_i \int d^3\mathbf{k}_s \int d^3\mathbf{k}_p\, \delta(\Delta\omega)\delta(\mathbf{q}_s + \mathbf{q}_i - \mathbf{q}_p) \\
\times \operatorname{sinc}\left(\frac{L_z}{2}\Delta k_z\right)\alpha_p(\mathbf{k}_p)\hat{a}_s^\dagger(\mathbf{k}_s)\hat{a}_i^\dagger(\mathbf{k}_i) + \mathrm{H.c.}
\end{aligned} \tag{A3}$$

The frequency of each field is dependent only on the modulus of the wave vector (and its polarization, assuming close to colinear propagation). Furthermore, we need to consider fields only with positive z components, which invites a change of integration variables from Cartesian components of $\mathbf{k}$ to transverse wave vector, $\mathbf{q}$, and the modulus of the wave vector, $|\mathbf{k}|$. Note that such a coordinate change results in a lack of clear correspondence of the mode operators to their strictly orthonormal counterparts; however, this mathematical convenience remains suitable for obtaining a description of the biphoton state. Hence, we can express the z components of the $\mathbf{k}$ in terms of their modulus and transverse components,

$$k_z = \sqrt{|\mathbf{k}|^2 - |\mathbf{q}|^2} = |\mathbf{k}|\sqrt{1 - \frac{|\mathbf{q}|^2}{|\mathbf{k}|^2}} \simeq |\mathbf{k}|\left(1 - \frac{1}{2}\frac{|\mathbf{q}|^2}{|\mathbf{k}|^2} - \frac{1}{8}\frac{|\mathbf{q}|^4}{|\mathbf{k}|^4} + O\left(\frac{|\mathbf{q}|^6}{|\mathbf{k}|^6}\right)\right), \tag{A4}$$

where we make use of a close-to-colinear approximation, $|\mathbf{q}| \ll |\mathbf{k}|$. Differentiating with respect to $|\mathbf{k}|$, we have

$$dk_z = \left(1 - \frac{|\mathbf{q}|^2}{|\mathbf{k}|^2}\right)^{-1/2} d|\mathbf{k}| \simeq \left(1 + \frac{1}{2}\frac{|\mathbf{q}|^2}{|\mathbf{k}|^2} + O\left(\frac{|\mathbf{q}|^4}{|\mathbf{k}|^4}\right)\right)d|\mathbf{k}|, \tag{A5}$$

allowing the transformation

$$d^3\mathbf{k} = d^2\mathbf{q}\, dk_z \approx d^2\mathbf{q}\, d|\mathbf{k}|\left(1 + \frac{1}{2}\frac{|\mathbf{q}|^2}{|\mathbf{k}|^2}\right). \tag{A6}$$

The phase-matching contribution arising from the longitudinal wave-vector mismatch can now be expressed as

$$\begin{aligned}
\Delta k_z &= k_{sz} + k_{iz} - k_{pz} + \frac{2\pi}{\Lambda} \\
&= \sqrt{|\mathbf{k}_s|^2 - |\mathbf{q}_s|^2} + \sqrt{|\mathbf{k}_i|^2 - |\mathbf{q}_i|^2} - \sqrt{|\mathbf{k}_p|^2 - |\mathbf{q}_p|^2} + \frac{2\pi}{\Lambda} \\
&= |\mathbf{k}_s|\sqrt{1 - \frac{|\mathbf{q}_s|^2}{|\mathbf{k}_s|^2}} + |\mathbf{k}_i|\sqrt{1 - \frac{|\mathbf{q}_i|^2}{|\mathbf{k}_i|^2}} - |\mathbf{k}_p|\sqrt{1 - \frac{|\mathbf{q}_p|^2}{|\mathbf{k}_p|^2}} + \frac{2\pi}{\Lambda} \\
&\approx |\mathbf{k}_s| + |\mathbf{k}_i| - |\mathbf{k}_p| - \frac{1}{2}\left[\frac{|\mathbf{q}_s|^2}{|\mathbf{k}_s|} + \frac{|\mathbf{q}_i|^2}{|\mathbf{k}_i|} - \frac{|\mathbf{q}_p|^2}{|\mathbf{k}_p|}\right] + \frac{2\pi}{\Lambda}.
\end{aligned} \tag{A7}$$

To proceed, we make use of the dispersion relations for the various fields, for which we make first-order expansions (no group velocity dispersion) about the degenerate, energy-matched frequencies $\omega_0 := \omega_{s0} = \omega_{i0} = \omega_{p0}/2$, so that, for the pump field,

$$|\mathbf{k}_p| = k_p^{(e)}(\omega_p) \simeq k_p^{(e)}(\omega_{p0}) + (\omega_p - \omega_{p0})\frac{1}{v_{gp}} = k_{p0} + \frac{\tilde{\omega}_p}{v_{gp}} = k_{p0} + \tilde{k}_p, \tag{A8}$$

where $k_p^{(e)}(\omega_p)$ is the dispersion relation for polarization on the extraordinary axis expanded about ω_{p0} (the central pump frequency), $\tilde{\omega}_p = (\omega_p - \omega_{p0})$ is the frequency offset, and v_{gp} and k_{p0} are the group velocity and wave vector of the pump field at ω_{p0}, polarized accordingly. Similarly, for signal and idler fields,

$$\begin{aligned} |\mathbf{k}_s| &= k_s^{(e)}(\omega_s) \simeq k_s^{(e)}(\omega_0) + (\omega_p - \omega_0)\frac{1}{v_{gs}} = k_{s0} + \frac{\tilde{\omega}_s}{v_{gs}} = k_{s0} + \tilde{k}_s, \\ |\mathbf{k}_i| &= k_i^{(o)}(\omega_i) \simeq k_i^{(o)}(\omega_0) + (\omega_i - \omega_0)\frac{1}{v_{gi}} = k_{i0} + \frac{\tilde{\omega}_i}{v_{gi}} = k_{i0} + \tilde{k}_i. \end{aligned} \tag{A9}$$

This allows us to consider the wave-vector mismatch for colinear generation ($\mathbf{q} \to 0$) at degeneracy ($\tilde{\omega} \to 0$),

$$\Delta k_{z0} := k_{s0} + k_{i0} - k_{p0}. \tag{A10}$$

Thus, rewriting Δk_z at degeneracy as

$$\Delta k_z = \Delta k_{z0} + \frac{2\pi}{\Lambda}. \tag{A11}$$

For sources optimized in this regime, periodic poling of the crystal is used to cancel this contribution, thereby achieving phase matching ($\Delta k_z = 0$). Thus, we set the poling period, $2\pi/\Lambda = -\Delta k_{z0}$.

Noting that we may write the energy-matching term as $\delta(\Delta\omega) = v_{gp}^{-1}\delta(v_{gs}\tilde{k}_s/v_{gp} + v_{gi}\tilde{k}_i/v_{gp} - \tilde{k}_p)$, then imposing the condition that the pump field may be expressed as a separable function of $\mathbf{q}$ and $\tilde{k}$ so that $\alpha_p(\mathbf{k}) \approx \alpha_p(\mathbf{q})\tilde{\alpha}_p(\tilde{k})$, and using the approximation made in Eq. (A6), we can perform the integrals $d^3\mathbf{k}_p$ in Eq. (A3) to arrive at the form

$$\begin{aligned} \int H^{\mathrm{NL}}(t)dt \propto & \int d^2\mathbf{q}_i d\tilde{k}_i \int d^2\mathbf{q}_s d\tilde{k}_s v_{gp}^{-1}\left(1 + \frac{1}{2}\frac{|\mathbf{q}_s|^2}{(k_{s0} + \tilde{k}_s)^2}\right)\left(1 + \frac{1}{2}\frac{|\mathbf{q}_i|^2}{(k_{i0} + \tilde{k}_i)^2}\right) \\ & \times \left(1 + \frac{1}{2}\frac{|\mathbf{q}_s + \mathbf{q}_i|^2}{(k_{p0} + v_{gs}\tilde{k}_s/v_{gp} + v_{gi}\tilde{k}_i/v_{gp})^2}\right) \\ & \times \operatorname{sinc}\left(\frac{L_z}{2}\left(\tilde{k}_s + \tilde{k}_i - \left(\frac{v_{gs}}{v_{gp}}\tilde{k}_s + \frac{v_{gi}}{v_{gp}}\tilde{k}_i\right)\right.\right. \\ & \left.\left. - \frac{1}{2}\left[\frac{|\mathbf{q}_s|^2}{k_{s0} + \tilde{k}_s} + \frac{|\mathbf{q}_i|^2}{k_{i0} + \tilde{k}_i} - \frac{|\mathbf{q}_s + \mathbf{q}_i|^2}{k_{p0} + v_{gs}\tilde{k}_s/v_{gp} + v_{gi}\tilde{k}_i/v_{gp}}\right]\right)\right) \\ & \times \alpha_p(\mathbf{q}_s + \mathbf{q}_i)\tilde{\alpha}_p\left(\frac{v_{gs}}{v_{gp}}\tilde{k}_s + \frac{v_{gi}}{v_{gp}}\tilde{k}_i\right)\hat{a}_s^\dagger(\mathbf{k}_s)\hat{a}_i^\dagger(\mathbf{k}_i) + \mathrm{H.c.} \end{aligned} \tag{A12}$$

Even for relatively broadband fields we have $\tilde{k} \ll k_0$ for the pump, signal, and idler, so we can approximate $\tilde{k} + k_0 \approx k_0$ in the sinc quotients, and for close to colinear generation, $|\mathbf{q}_i|^2/(k_{i0} + \tilde{k}_i)^2 \ll 1$, so we can neglect polynomial terms in front of the sinc of the order $\mathcal{O}(|\mathbf{q}|^2/k_0^2)$ and above, to obtain

$$\begin{aligned} \int H^{\mathrm{NL}}(t)dt \propto & \int d^2\mathbf{q}_i d\tilde{k}_i \int d^2\mathbf{q}_s d\tilde{k}_s \\ & \times \operatorname{sinc}\left(\frac{L_z}{2}\left(\tilde{k}_s + \tilde{k}_i - \left(\frac{v_{gs}}{v_{gp}}\tilde{k}_s + \frac{v_{gi}}{v_{gp}}\tilde{k}_i\right) - \frac{1}{2}\left[\frac{|\mathbf{q}_s|^2}{k_{s0}} + \frac{|\mathbf{q}_i|^2}{k_{i0}} - \frac{|\mathbf{q}_s + \mathbf{q}_i|^2}{k_{p0}}\right]\right)\right) \\ & \times \alpha_p(\mathbf{q}_s + \mathbf{q}_i)\tilde{\alpha}_p\left(\frac{v_{gs}}{v_{gp}}\tilde{k}_s + \frac{v_{gi}}{v_{gp}}\tilde{k}_i\right)\hat{a}_s^\dagger(\mathbf{k}_s)\hat{a}_i^\dagger(\mathbf{k}_i) + \mathrm{H.c.} \end{aligned} \tag{A13}$$

At degeneracy, where $\tilde{k}_s = \tilde{k}_i = 0$, we have

$$\int H^{\rm NL}(t)dt \propto \int d^2\mathbf{q}_i d\tilde{k}_i \int d^2\mathbf{q}_s d\tilde{k}_s \,\mathrm{sinc}\left(\frac{L_z}{4}\left[\frac{|\mathbf{q}_s+\mathbf{q}_i|^2}{k_{p0}} - \frac{|\mathbf{q}_s|^2}{k_{s0}} - \frac{|\mathbf{q}_i|^2}{k_{i0}}\right]\right) \times \alpha_p(\mathbf{q}_s+\mathbf{q}_i)\hat{a}_s^\dagger(\mathbf{k}_s)\hat{a}_i^\dagger(\mathbf{k}_i) + \text{H.c.} \tag{A14}$$

To simplify further, we define a scaled transverse momenta

$$\tilde{\mathbf{q}}_s := \left(\frac{k_{p0}}{k_{s0}} - 1\right)^{1/2}\mathbf{q}_s := c_s\mathbf{q}_s, \tag{A15}$$

and analogously for the idler. We write $\varepsilon := 1 - 1/c_s c_i$ and express the product of the sinc function and pump profile α_p as

$$F(\mathbf{q}_s,\mathbf{q}_i) \propto \mathrm{sinc}\left(\frac{L_z}{4k_{p0}}[(2+\varepsilon)|\tilde{\mathbf{q}}_-|^2 + \varepsilon|\tilde{\mathbf{q}}_+|^2]\right)\alpha_p(\mathbf{q}_s+\mathbf{q}_i), \tag{A16}$$

where $|\tilde{\mathbf{q}}_\pm| := |c_s\mathbf{q}_s \pm c_i\mathbf{q}_i|/\sqrt{2}$. We define the above expression as the JTMA.

For $\lambda_s = 1550$ nm, we have $c_s = 0.9677$, $c_i = 1.0139$ and, for $\lambda_s = 810$ nm, $c_s = 0.9979$, $c_i = 1.047$. We approximate $\varepsilon \approx 0$ because $\varepsilon = -0.0193$ at 1550 nm and $\varepsilon = 0.043$ at 810 nm. Under this approximation, the JTMA can be simplified to

$$F(\mathbf{q}_s,\mathbf{q}_i) \propto \mathrm{sinc}\left(\frac{L_z}{2k_{p0}}|\tilde{\mathbf{q}}_-|^2\right)\alpha_p(\mathbf{q}_s+\mathbf{q}_i). \tag{A17}$$

We see that colinear type-II phase matching with periodic poling deviates somewhat from the idealized JTMA in the main text [Eq. (1)] owing to the nonunit c_s, c_i, and the nonvanishing ε. However, this discrepancy becomes increasingly benign for the collection-limited systems in consideration where the sinc contribution becomes dominated instead by the collection optics.

Rewriting the normalized JTMA for $c_s = c_i \approx 1$ (and remaining at degeneracy $\lambda_s = \lambda_i$), we impose a Gaussian transverse pump profile across the crystal, to obtain

$$F(\mathbf{q}_s,\mathbf{q}_i) = \mathcal{N}_1\mathrm{sinc}\left(\frac{|\mathbf{q}_s-\mathbf{q}_i|^2}{\sigma_S^2}\right)\exp\left(-\frac{|\mathbf{q}_s+\mathbf{q}_i|^2}{2\sigma_P^2}\right), \tag{A18}$$

where $\sigma_S = \sqrt{4k_{p0}/L_z}$ and $\mathcal{N}_1$ is a normalization constant. Here the transverse pump momentum profile $\alpha_P(\mathbf{q}_p)$ is a Gaussian, where w_P is the pump radius in position space, so that $\sigma_P = \sqrt{2}/w_P$.

Transforming to the Fourier plane with a $2f$ -lens configuration, we have ($\mathbf{q} \to 2\pi\mathbf{x}/f\lambda$),

$$F(\mathbf{x}_s,\mathbf{x}_i) \propto \mathrm{sinc}\left(\frac{1}{\sigma_S^2}\left|\frac{2\pi}{f\lambda_s}\mathbf{x}_s - \frac{2\pi}{f\lambda_i}\mathbf{x}_i\right|^2\right)\alpha_p\left(-\frac{1}{2\sigma_P^2}\left|\frac{2\pi}{f\lambda_s}\mathbf{x}_s + \frac{2\pi}{f\lambda_i}\mathbf{x}_i\right|^2\right). \tag{A19}$$

APPENDIX B: COLLECTED JTMA TO COLLECTION-LIMITED JTMA

We introduce the effect of the collection mode in $F(\mathbf{q}_s,\mathbf{q}_i)$ by considering collected JTMA $G(\mathbf{q}_+,\mathbf{q}_-)$ given in Eq. (7). To approximate the collected JTMA to the collection-limited JTMA, the product of the sinc term and the collection Gaussian envelope,

$$f(|\mathbf{q}_-|) = \mathcal{N}\exp\left\{\frac{-|\mathbf{q}_-|^2}{\sigma_C^2}\right\}\mathrm{sinc}\left(\frac{2|\mathbf{q}_-|^2}{\sigma_S^2}\right) \tag{B1}$$

with $\mathcal{N}$ a normalization factor, is approximated by the Gaussian function

$$g(|\mathbf{q}_-|) = \mathcal{N}'\exp\left\{\frac{-|\mathbf{q}_-|^2}{\sigma_C^2}\right\}. \tag{B2}$$

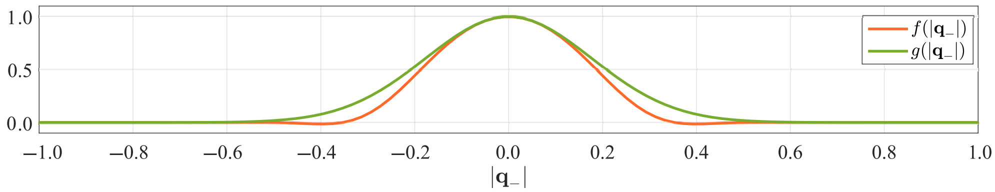

FIG. 7. Comparison between the product of the sinc and Gaussian term ($f(|\mathbf{q}_-|)$) and the collection Gaussian envelope ($g(|\mathbf{q}_-|)$). For $\sigma_S \gtrapprox \sqrt{2}\sigma_C$, the product of the sinc term and Gaussian envelope can be approximated by a Gaussian with width σ_C.

These terms have inner product

$$\int d^2\mathbf{q}_- \mathcal{N} \exp\left\{\frac{-|\mathbf{q}_-|^2}{\sigma_C^2}\right\} \mathrm{sinc}\left(\frac{2|\mathbf{q}_-|^2}{\sigma_S^2}\right) \mathcal{N}' \exp\left\{\frac{-|\mathbf{q}_-|^2}{\sigma_C^2}\right\} \geq 0.99 \tag{B3}$$

for $\sigma_S > 1.4161\sigma_C \gtrapprox \sqrt{2}\sigma_C$ (as shown in Fig. 7). A slightly looser approximation sees an inner product of 0.95 achieved at $\sigma_S > 3\sigma_C/2\sqrt{2}$.

Furthermore, in the case of calculating the single count rates in Eq. (15), in which only the herald photon imparts a collection envelope, we have a mildly stronger condition for the approximation to hold,

$$\mathcal{N} \exp\left\{\frac{-|\mathbf{q}_-|^2}{2\sigma_C^2}\right\} \mathrm{sinc}\left(\frac{2|\mathbf{q}_-|^2}{\sigma_S^2}\right) \approx \mathcal{N}' \exp\left\{\frac{-|\mathbf{q}_-|^2}{2\sigma_C^2}\right\}, \tag{B4}$$

leading to an additional factor of $\sqrt{2}$ arising in the equivalent conditions above, i.e., $\sigma_S \gtrapprox 2\sigma_C$ implies a greater than 0.99 inner product.

APPENDIX C: CALCULATIONS OF Pr$(a, -a)$ AND Pr(a, a)

For convenience, the expression for the two-photon coincidence probability in Eq. (6) can be written in the reduced form

$$\Pr(a_s, a_i) = |G_{++} + G_{--} - G_{-+} - G_{+-}|^2. \tag{C1}$$

For the signal photon, subscript "+" represents the integration performed in the $[a_s, \infty)$ interval and subscript "−" corresponds to the integration performed in the $(-\infty, a_s]$ interval (same for the idler).

To calculate $\Pr(a, -a)$, we expand the integral for $\Pr(a, -a)$ in terms of integrals over regions G_{++}^{CL}, G_{--}^{CL}, G_{-+}^{CL}, and G_{+-}^{CL} [see Fig. 8(a)]. From symmetry, we have $G_{--}^{\mathrm{CL}} = G_{++}^{\mathrm{CL}}$, and with Eq. (C1) we write $\Pr(a, -a)$ as

$$\Pr(a, -a) = |N - 4G_{--}^{\mathrm{CL}}|^2, \tag{C2}$$

where $N = G_{--}^{\mathrm{CL}} + G_{++}^{\mathrm{CL}} + G_{-+}^{\mathrm{CL}} + G_{+-}^{\mathrm{CL}} = \pi\sqrt{2\pi}\mathcal{N}_1\sigma_C^3\sigma_P^2/(\sigma_C^2 + \sigma_P^2)$. Assuming the $\sigma_P \ll \sigma_C$ in the bow-tie region formed by G_{--}^{CL} and G_{++}^{CL}, the factor $\exp\{-(q_{sx} - q_{ix})^2/2\sigma_C^2\}$ is approximated by $\exp(-2a^2/\sigma_C^2)$, which reduces the expression in Eq. (C2) to

$$\Pr(a, -a) \approx \left| N - 4\int_{-\infty}^{a}\int_{-\infty}^{-a} \mathcal{G}^{\mathrm{DG}}(q_{sx}, q_{ix}; a) dq_{sx} dq_{ix} \right|^2, \tag{C3}$$

where

$$\mathcal{G}^{\mathrm{DG}}(q_{sx}, q_{ix}; a) \propto \exp\left(-\frac{(q_{sx} + q_{ix})^2}{2\tilde{\sigma}_P^2}\right) \exp\left(-\frac{2a^2}{\sigma_C^2}\right), \tag{C4}$$

for which there exists a simple analytic solution

$$\Pr(a,-a) \approx \left|N - N' \exp\left(-\frac{2a^2}{\sigma_C^2}\right)\right|^2,$$
$$N' := \sqrt{2\pi}\mathcal{N}_1 \frac{\pi\sigma_C^3\sigma_P^3}{(\sigma_C^2+\sigma_P^2)^{3/2}}, \tag{C5}$$

given in Eq. (9). One can write the expression for the visibility V in terms of N and N' as

$$V = \frac{|N|^2 - |N-N'|^2}{|N|^2 + |N-N'|^2} \approx \frac{\sigma_C^2 - |\sigma_C - \sigma_P|^2}{\sigma_C^2 + |\sigma_C - \sigma_P|^2} \quad \text{for } \sigma_P \ll \sigma_C. \tag{C6}$$

For a fixed value of σ_C, obtained from the fit of $\Pr(a,-a)$, one can also get the pump width parameter σ_P from Eq. (C6), given the visibility of the experimental data.

Therefore, for $\Pr(a,a)$, we follow the same steps as $\Pr(a,-a)$ of writing the complete integral as the sum of integrals over several regions [see Fig. 8(b)]. Here, the integrals G_{-+}^{CL} and G_{+-}^{CL} are equal ($G_{+-}^{\mathrm{CL}} = G_{-+}^{\mathrm{CL}} \equiv \tilde{R}$). We aim to partition the space into areas that have closed-form integral solutions and a bow-tie region that can be well approximated under the previous reasoning. We expand $\tilde{R} = \tilde{E} + F - (\tilde{F}_1 + \tilde{F}_2)$, where the contributions are given as

$$\tilde{E} = \iint_{\mathcal{L}} G^{\mathrm{CL}}(q_{+x}, q_{-x})dq_{+x}dq_{-x}, \tag{C7a}$$

$$F = \frac{1}{2}\int_a^{3a}\int_{-a}^{a} \mathcal{G}^{\mathrm{DG}}(q_{sx}, q_{ix}; a)dq_{sx}dq_{ix}, \tag{C7b}$$

$$\tilde{F}_1 = \frac{1}{2}\int_{-\infty}^{a}\int_{-\infty}^{-a} \mathcal{G}^{\mathrm{DG}}(q_{sx}, q_{ix}; a)dq_{sx}dq_{ix}, \tag{C7c}$$

$$\tilde{F}_2 = \frac{1}{2}\int_{3a}^{\infty}\int_{a}^{\infty} \mathcal{G}^{\mathrm{DG}}(q_{sx}, q_{ix}; a)dq_{sx}dq_{ix}, \tag{C7d}$$

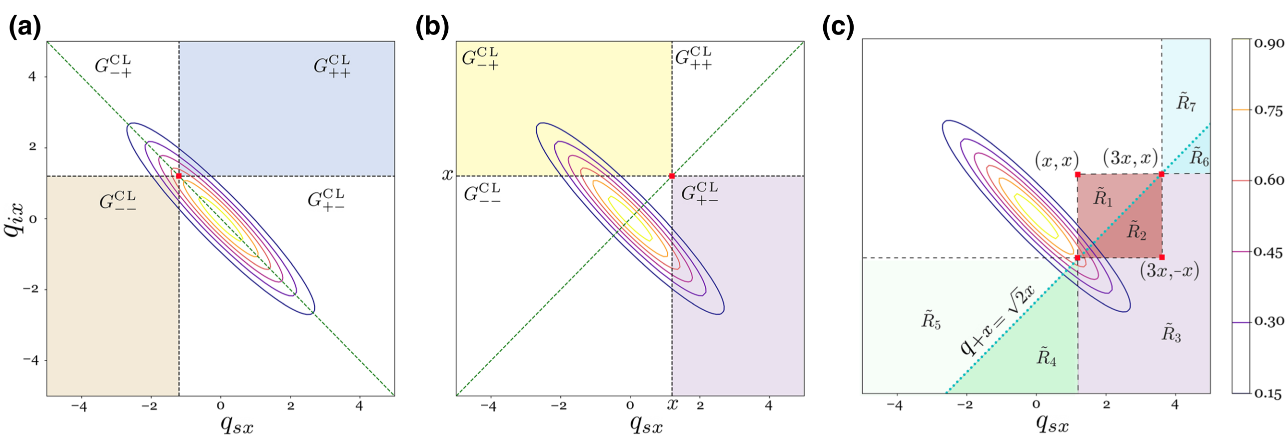

FIG. 8. Illustration of the regions in collected JTMA to approximate $\Pr(a,-a)$ and $\Pr(a,a)$. (a) For $\Pr(a,-a)$, the shaded regions G_{++}^{CL} and G_{--}^{CL} are equal due to the symmetry about $q_{+x} = 0$ (green, dashed). (b) Similarly, for $\Pr(a,a)$, the regions G_{-+}^{CL} and G_{+-}^{CL} are equal due to symmetry across $q_{-x} = 0$. In (c) $G_{+-}^{\mathrm{CL}} = \tilde{R}_1 + \tilde{R}_2 + \tilde{R}_3$, which is calculated from various integrals [see Eqs. (C7) and (C8)].

where $G^{\mathrm{CL}}(q_{+x}, q_{-x})$ is integrated over the region $\mathcal{L} \in (q_{-x} \leq \sqrt{2}x)$. The rationale behind this expansion can be seen when we further express each terms in the sum of $\tilde{R}$ into the regions shown in Fig. 8(c),

$$\tilde{E} = \tilde{R}_2 + \tilde{R}_3 + \tilde{R}_4 + \tilde{R}_6, \qquad F = \tfrac{1}{2}(\tilde{R}_1 + \tilde{R}_2) = \tilde{R}_1, \tag{C8a}$$

$$\tilde{F}_1 = \tfrac{1}{2}(\tilde{R}_5 + \tilde{R}_4) = \tilde{R}_4, \qquad \tilde{F}_2 = \tfrac{1}{2}(\tilde{R}_7 + \tilde{R}_6) = \tilde{R}_6, \tag{C8b}$$

$$\tilde{R} = \tilde{E} + F - (\tilde{F}_1 + \tilde{F}_2) = \tilde{R}_1 + \tilde{R}_2 + \tilde{R}_3. \tag{C8c}$$

We solve for $N - 4\tilde{R}$ with the help of integral tables given for error functions and the fact that $\Pr(a, a)$ is an even function, and we get

$$N - 4\tilde{R} = \mathcal{A}\left[\sqrt{2}\sigma_P e^{-2a^2(1/\tilde{\sigma}_P^2 + 1/\sigma_C^2)} - 2\sqrt{\pi}\,|a| e^{-2a^2/\sigma_C^2} \operatorname{erfc}\left(\frac{\sqrt{2}|a|}{\tilde{\sigma}_P}\right) - \frac{\pi\sigma_C}{2\sqrt{2}}\left\{1 - 2\operatorname{erf}\left(\frac{\sqrt{2}|a|}{\sigma_C}\right)\right\}\right]. \tag{C9}$$

To fit $\Pr(a, -a)$ and $\Pr(a, a)$, one requires the estimated location of the origin from the experiment data, which we can obtain from

$$\Pr(a, -\infty) \propto \left|\operatorname{erf}\left(\frac{\sqrt{2}(a - a_s)}{\sigma_C}\right)\right|^2, \qquad \Pr(-\infty, a) \propto \left|\operatorname{erf}\left(\frac{\sqrt{2}(a - a_i)}{\sigma_C}\right)\right|^2, \tag{C10}$$

where $\Pr(a, -\infty)$ is minimum for $a = a_s$ [$\Pr(-\infty, a)$ is minimum for $a = a_i$]. Hence, the location of the origin coincides with the locations of the respective minima ($q_{sx} = a_s, q_{ix} = a_i$).

APPENDIX D: MODE BASIS DESIGN AND HERALDING EFFICIENCY DETAILS

To produce a postselected state experimentally, we project holograms $\{\Phi_s(\mathbf{q}_s)\}_a$ and $\{\Phi_i(\mathbf{q}_i)\}_b$ on the SLMs with an additional constraint $|\Phi_s(\mathbf{q}_s)| \leq 1$. This results in a state characterized by the complex elements T_{ab} given by

$$T_{ab} = \int d^2\mathbf{q}_s \int d^2\mathbf{q}_i \Phi_s^a(\mathbf{q}_s)\Phi_i^b(\mathbf{q}_i) G(\mathbf{q}_s, \mathbf{q}_i). \tag{D1}$$

The subnormalized postselected state, $|\psi^{(\mathrm{PS})}\rangle$, which is defined on the corresponding normalized discrete mode basis $\{|\hat{e}_s^a\rangle\}_a$ is given by,

$$|\psi^{(\mathrm{PS})}\rangle := \sum_{ab} T_{ab}\,|\hat{e}_s^a\rangle\,|\hat{e}_i^b\rangle\,, \tag{D2}$$

where, to ensure $\{|\hat{e}_s^a\rangle\}_a$ are normalized, we write

$$|\langle\hat{e}_s^a|\hat{e}_s^a\rangle|^2 = 1 = N_s^a\left|\int d^2\mathbf{q}_s \Phi_s^a(\mathbf{q}_s)\mathcal{C}(\mathbf{q}_s|\sigma_C)\right|^2 = N_s^a\left|\int d^2\mathbf{q}_s M_s^a(\mathbf{q}_s)\right|^2 \tag{D3}$$

with N_s^a a normalization factor (similar for the idler). We construct the holograms so that $|\hat{e}_n^a\rangle$ ($n = s, i$) are orthogonal and form the discrete mode basis, which can be easily achieved by, for instance, making $\{\Phi_s(\mathbf{q}_s)\}_a$ disjoint (pixels). The resultant state can be understood as the full biphoton state filtered through the collection mode apertures defined by $\hat{L}_s$ and $\hat{L}_i$,

$$\begin{aligned}\hat{L}_s &:= \sum_a \frac{1}{\sqrt{N_s^a}}|\hat{e}_s^a\rangle\langle\hat{e}_s^a|,\\ |\psi^{(\mathrm{PS})}\rangle &:= \hat{L}_s\hat{L}_i\,|\psi^{(bi)}\rangle\,.\end{aligned} \tag{D4}$$

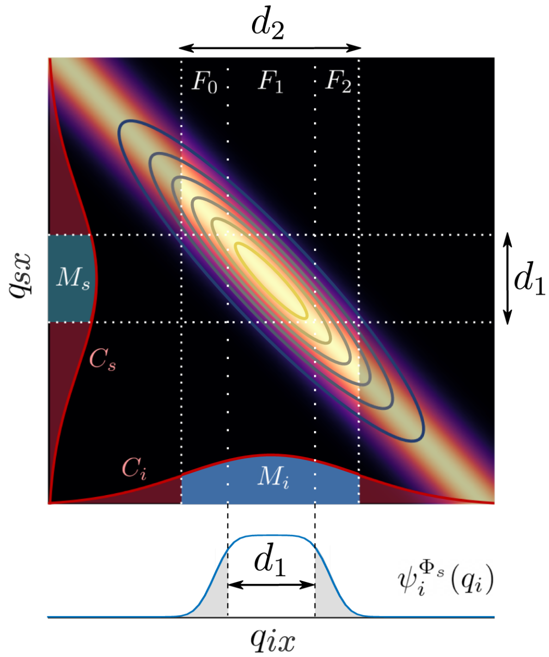

FIG. 9. Heralding of the idler photon state by projection onto a signal photon. The signal photon is projected onto the measurement mode $M_s(\mathbf{q}_s) = \Phi_s(\mathbf{q}_s)\mathcal{C}(\mathbf{q}_s|\sigma_C)$ (turquoise, left axis) determined by the collection mode $\mathcal{C}_s$ (red, left axis) and a pixel hologram Φ_s, of diameter d_1. The resultant heralded idler photon state $\psi_i^{\Phi_s}(\mathbf{q}_i)$ (blue, bottom) is determined by the projection of $M_s(\mathbf{q}_s)$ onto the JTMA (contours) [see Eq. (D7)], which, owing to the relative size of σ_C, can be approximated by the correlation term (density plot) (see Appendix B). The finite width of the JTMA leads to contributions arising from regions F_0 and F_2 that result in a heralded photon with a width larger than d_1. The idler measurement mode, $M_i(\mathbf{q}_i) = \Phi_i(\mathbf{q}_i)\mathcal{C}(\mathbf{q}_i|\sigma_C)$ (blue region, lower plot axes) is chosen to have an increased pixel diameter $d_2 > d_1$, leading to an increased coincidence probability given by the inner product $\langle M_i^{\Phi_s}, \psi_i^{\Phi_s}\rangle$ [Eq. (D9)], whilst the (inclusive) singles probability of the signal detection is $\langle \psi_i^{\Phi_s}, \psi_i^{\Phi_s}\rangle$ [Eq. (D7)], independent of d_2. Hence, an increased d_2 leads to an increase in the one-sided heralding efficiency [Eq. (17)].

When measuring arbitrary vectors in this subspace, for instance $|\vec{v}^s\rangle = \sum_a v_a^s |\hat{e}^a\rangle$, with $|\langle\vec{v}^s|\vec{v}^s\rangle| = 1$, one constructs the holograms as

$$\Phi_s^{\vec{v}}(\mathbf{q}_s) = A^{\vec{v}} \sum_a v_a \Phi_s^a(\mathbf{q}_s) \tag{D5}$$

with $A^{\vec{v}}$ chosen so that $\max_{\mathbf{q}} |\Phi_s^{\vec{v}}(\mathbf{q})| \leq 1$. These holograms result in the measurement statistics

$$\Pr(\vec{v}^s, \vec{v}^i) = (A^{\vec{v}^s} A^{\vec{v}^i})^2 |\langle \vec{v}^s | \langle \vec{v}^i | | \psi^{(\mathrm{PS})}\rangle|^2. \tag{D6}$$

The choice of $A^{\vec{v}}$ results in an effective change in the postselection probability. Similarly, the probability of obtaining a (inclusive) single signal photon when measuring these states is

$$\psi_i^{\Phi_s}(\mathbf{q}_i) := \int d^2\mathbf{q}_s \Phi_s^{\vec{v}^s}(\mathbf{q}_s)\mathcal{C}(\mathbf{q}_s|\sigma_C)F(\mathbf{q}_s, \mathbf{q}_i), \tag{D7}$$

$$\begin{aligned}\Pr(\vec{v}^s) &= \int d^2\mathbf{q}_i |\psi_i^{\Phi_s}(\mathbf{q}_i)|^2 \\ &= (A^{\vec{v}^s})^2 \int d^2\mathbf{q}_i |\langle \vec{v}^s | \langle \mathbf{q}_i | \hat{L}_s | \psi^{bi}\rangle|^2,\end{aligned} \tag{D8}$$

with $\psi_i^{\Phi_s}(\mathbf{q}_i)$ describing the pure heralded idler photon state after heralding with $\Phi_s^{\vec{v}^s}$ on the signal. The coincidence probability can be written similarly in terms of this heralded idler photon state,

$$\Pr(\vec{v}^s, \vec{v}^i) = \left| \int d^2\mathbf{q}_i M_i^{\Phi_s}(\mathbf{q}_i)\psi_i^{\Phi_s}(\mathbf{q}_i)\right|^2. \tag{D9}$$

The one-sided heralding efficiency is given by

$$\eta^{s\to i} = \frac{\Pr(\vec{v}^s, \vec{v}^i)}{\Pr(\vec{v}^s)}, \tag{D10}$$

which can be optimized by ensuring that the idler mode basis has large overlap with the heralded photons from the signal, as well as choosing measurements for which $A^{\vec{v}_i}$ may be large. In Fig. 9 we depict the increased heralding efficiency associated with increasing the size of one party's pixel relative to the other.

[1] A. Einstein, B. Podolsky, and N. Rosen, Can quantum-mechanical description of physical reality be considered complete?, Phys. Rev. **47**, 777 (1935).

[2] M. D. Reid, P. D. Drummond, W. P. Bowen, E. G. Cavalcanti, P. K. Lam, H. A. Bachor, U. L. Andersen, and G Leuchs, Colloquium: The Einstein-Podolsky-Rosen paradox: from concepts to applications, Rev. Mod. Phys. **81**, 1727 (2009).

[3] D. Bohm and Y. Aharonov, Discussion of experimental proof for the paradox of Einstein, Rosen, and Podolsky, Phys. Rev. **108**, 1070 (1957).

[4] John S. Bell, On the Einstein Podolsky Rosen paradox, Phys. Phys. Fiz. **1**, 195 (1964).

[5] Nicolas Brunner, Daniel Cavalcanti, Stefano Pironio, Valerio Scarani, and Stephanie Wehner, Bell nonlocality, Rev. Mod. Phys. **86**, 419 (2014).

[6] John Clauser, Michael Horne, Abner Shimony, and Richard Holt, Proposed Experiment to Test Local Hidden-Variable Theories, Phys. Rev. Lett. **23**, 880 (1969).

[7] Alain Aspect, Philippe Grangier, and Gérard Roger, Experimental Realization of Einstein-Podolsky-Rosen-Bohm Gedankenexperiment: A New Violation of Bell's Inequalities, Phys. Rev. Lett. **49**, 91 (1982).

[8] D. K. Shin, B. M. Henson, S. S. Hodgman, Tomasz Wasak, Jan Chwedeńczuk, and A.G. Truscott, Bell correlations between spatially separated pairs of atoms, Nat. Commun. **10**, 4447 (2019).

[9] Tomasz Wasak and Jan Chwedeńczuk, Bell Inequality, Einstein-Podolsky-Rosen Steering, and Quantum Metrology with Spinor Bose-Einstein Condensates, Phys. Rev. Lett. **120**, 140406 (2018).

[10] Michael Keller, Mateusz Kotyrba, Florian Leupold, Mandip Singh, Maximilian Ebner, and Anton Zeilinger, Bose-Einstein condensate of metastable helium for quantum correlation experiments, Phys. Rev. A **90**, 063607 (2014).

[11] Bienvenu Ndagano, Hugo Defienne, Ashley Lyons, Ilya Starshynov, Federica Villa, Simone Tisa, and Daniele Faccio, Imaging and certifying high-dimensional entanglement with a single-photon avalanche diode camera, npj Quantum Inf. **6**, 94 (2020).

[12] M. P. Edgar, D. S. Tasca, F Izdebski, R. E. Warburton, J Leach, M Agnew, G. S. Buller, R. W. Boyd, and Miles J Padgett, Imaging high-dimensional spatial entanglement with a camera, Nat. Commun. **3**, 984 (2012).

[13] Paul-Antoine Moreau, Joé Mougin-Sisini, Fabrice Devaux, and Eric Lantz, Realization of the purely spatial Einstein-Podolsky-Rosen paradox in full-field images of spontaneous parametric down-conversion, Phys. Rev. A **86**, 010101 (2012).

[14] Robert W. Boyd, *Nonlinear Optics* (Academic Press, Boston, 2008).

[15] C. K. Hong and L. Mandel, Theory of parametric frequency down conversion of light, Phys. Rev. A **31**, 2409 (1985).

[16] A. Malygin, A. Penin, and Alexander Sergienko, *Spatiotemporal grouping of photons in spontaneous parametric scattering of light*, Sov. Phys. Dokl.1985.

[17] James Schneeloch and John C Howell, Introduction to the transverse spatial correlations in spontaneous parametric down-conversion through the biphoton birth zone, J. Opt. **18**, 53501 (2016).

[18] E. Brambilla, L. Caspani, L. A. Lugiato, and A. Gatti, Spatiotemporal structure of biphoton entanglement in type-II parametric down-conversion, Phys. Rev. A **82**, 013835 (2010).

[19] S. P. Walborn, C. H. Monken, S. Pádua, and P. H. Souto Ribeiro, Spatial correlations in parametric down-conversion, Phys. Rep. **495**, 87 (2010).

[20] Mario Krenn, Mehul Malik, Manuel Erhard, and Anton Zeillinger, Orbital angular momentum of photons and the entanglement of Laguerre-Gaussian modes, Phil. Trans. R Soc. A **375**, 20150442 (2017).

[21] Manuel Erhard, Mario Krenn, and Anton Zeilinger, Advances in high dimensional quantum entanglement, Nat. Rev. Phys. **2**, 365 (2020).

[22] Nicolai Friis, Giuseppe Vitagliano, Mehul Malik, and Marcus Huber, Entanglement certification from theory to experiment, Nat. Rev. Phys. **1**, 72 (2019).

[23] Daniel Collins, Nicolas Gisin, Noah Linden, Serge Massar, and Sandu Popescu, Bell Inequalities for Arbitrarily High-Dimensional Systems, Phys. Rev. Lett. **88**, 040404 (2002).

[24] Alexia Salavrakos, Remigiusz Augusiak, Jordi Tura, Peter Wittek, Antonio Acín, and Stefano Pironio, Bell Inequalities Tailored to Maximally Entangled States, Phys. Rev. Lett. **119**, 040402 (2017).

[25] Adetunmise C. Dada, Jonathan Leach, Gerald S. Buller, Miles J. Padgett, and Erika Andersson, Experimental high-dimensional two-photon entanglement and violations of generalized Bell inequalities, Nat. Phys. **7**, 677 (2011).

[26] Jessica Bavaresco, Natalia Herrera Valencia, Claude Klockl, Matej Pivoluska, Paul Erker, Nicolai Friis, Mehul Malik, and Marcus Huber, Measurements in two bases are sufficient for certifying high-dimensional entanglement, Nat. Phys. **14**, 1032 (2018).

[27] Xi-Lin Wang, Xin-Dong Cai, Zu-En Su, Ming-Cheng Chen, Dian Wu, Li Li, Nai-Le Liu, Chao-Yang Lu, and Jian-Wei Pan, Quantum teleportation of multiple degrees of freedom of a single photon, Nature **518**, 516 (2015).

[28] Mehul Malik, Manuel Erhard, Marcus Huber, Mario Krenn, Robert Fickler, and Anton Zeilinger, Multi-photon entanglement in high dimensions, Nat. Photonics **10**, 248 (2016).

[29] Manuel Erhard, Mehul Malik, Mario Krenn, and Anton Zeilinger, Experimental Greenberger-Horne-Zeilinger entanglement beyond qubits, Nat. Photon **12**, 759 (2018).

[30] B. C. Hiesmayr, M. J. A. de Dood, and W. Löffler, Observation of Four-Photon Orbital Angular Momentum Entanglement, Phys. Rev. Lett. **116**, 073601 (2016).

[31] Xiao-Min Hu, Wen-Bo Xing, Chao Zhang, Bi-Heng Liu, Matej Pivoluska, Marcus Huber, Yun-Feng Huang, Chuan-Feng Li, and Guang-Can Guo, Experimental creation of multi-photon high-dimensional layered quantum states, npj Quantum Inf. **6**, 88 (2020).

[32] Natalia Herrera Valencia, Suraj Goel, Will McCutcheon, Hugo Defienne, and Mehul Malik, Unscrambling entanglement through a complex medium, Nat. Phys. **16**, 1112 (2020).

[33] Huan Cao, She-Cheng Gao, Chao Zhang, Jian Wang, De-Yong He, Bi-Heng Liu, Zheng-Wei Zhou, Yu-Jie Chen, Zhao-Hui Li, Si-Yuan Yu, Jacquiline Romero, Yun-Feng Huang, Chuan-Feng Li, and Guang-Can Guo, Distribution of high-dimensional orbital angular momentum entanglement over a 1 km few-mode fiber, Optica **7**, 232 (2020).

[34] Daniele Cozzolino, Beatrice Da Lio, Davide Bacco, and Leif Katsuo Oxenløwe, High-dimensional quantum communication: Benefits, progress, and future challenges, Adv. Quantum Technol. **2**, 1900038 (2019).

[35] Manuel Erhard, Mehul Malik, and Anton Zeilinger, A quantum router for high-dimensional entanglement, Quantum Sci. Technol. **2**, 014001 (2017).

[36] Fabian Steinlechner, Sebastian Ecker, Matthias Fink, Bo Liu, Jessica Bavaresco, Marcus Huber, Thomas Scheidl, and Rupert Ursin, Distribution of high-dimensional entanglement via an intra-city free-space link, Nat. Commun. **8**, 15971 (2017).

[37] Mhlambululi Mafu, Angela Dudley, Sandeep Goyal, Daniel Giovannini, Melanie McLaren, Miles J. Padgett, Thomas Konrad, Francesco Petruccione, Norbert Lütkenhaus, and Andrew Forbes, Higher-dimensional orbital-angular-momentum-based quantum key distribution with mutually unbiased bases, Phys. Rev. A **88**, 032305 (2013).

[38] Sebastian Ecker, Frédéric Bouchard, Lukas Bulla, Florian Brandt, Oskar Kohout, Fabian Steinlechner, Robert Fickler, Mehul Malik, Yelena Guryanova, Rupert Ursin, and Marcus Huber, Overcoming Noise in Entanglement Distribution, Phys. Rev. X **9**, 041042 (2019).

[39] F. Zhu, M. Tyler, N. H. Valencia, M. Malik, and J. Leach, Is high-dimensional photonic entanglement robust to noise? AVS Quantum Sci. **3**, 011401 (2021).

[40] Marcus Huber and Marcin Pawłowski, Weak randomness in device-independent quantum key distribution and the advantage of using high-dimensional entanglement, Phys. Rev. A **88**, 032309 (2013).

[41] Tamás Vertesi, Stefano Pironio, and Nicolas Brunner, Closing the Detection Loophole in Bell Experiments Using Qudits, Phys. Rev. Lett. **104**, 60401 (2010).

[42] Vatshal Srivastav, Natalia Herrera Valencia, Will McCutcheon, Saroch Leedumrongwatthanakun, Sébastien Designolle, Roope Uola, Nicolas Brunner, and Mehul Malik, Noise-robust and loss-tolerant quantum steering with qudits, (2022), ArXiv:2202.09294.

[43] Antonio Acín, Nicolas Brunner, Nicolas Gisin, Serge Massar, Stefano Pironio, and Valerio Scarani, Device-Independent Security of Quantum Cryptography against Collective Attacks, Phys. Rev. Lett. **98**, 230501 (2007).

[44] F. M. Miatto, H. D.i Lorenzo Pires, S. M. Barnett, and M. P. van Exter, Spatial Schmidt modes generated in parametric down-conversion, Eur. Phys. J. D **66**, 263 (2012).

[45] John C Howell, Ryan S Bennink, Sean J Bentley, and R. W. Boyd, Realization of the Einstein-Podolsky-Rosen Paradox Using Momentum- and Position-Entangled Photons from Spontaneous Parametric Down Conversion, Phys. Rev. Lett. **92**, 210403 (2004).

[46] J. Schneeloch, C. C. Tison, M. L. Fanto, Paul M. Alsing, and Gregory A. Howland, Quantifying entanglement in a 68-billion-dimensional quantum state space, Nat. Commun. **10**, 2785 (2019).

[47] Hugo Defienne, Matthew Reichert, and Jason W. Fleischer, General Model of Photon-Pair Detection with an Image Sensor, Phys. Rev. Lett. **120**, 203604 (2018).

[48] F. M. Miatto, D Giovannini, J Romero, S Franke-Arnold, S. M. Barnett, and M. J. Padgett, Bounds and optimisation of orbital angular momentum bandwidths within parametric down-conversion systems, Eur. Phys. J. D **66**, 178 (2012).

[49] Baghdasar Baghdasaryan, Fabian Steinlechner, and Stephan Fritzsche, Justifying the thin-crystal approximation in spontaneous parametric down-conversion for collinear phase matching, Phys. Rev. A **103**, 063508 (2021).

[50] Hammam Qassim, Filippo M. Miatto, Juan P. Torres, Miles J. Padgett, Ebrahim Karimi, and Robert W. Boyd, Limitations to the determination of a Laguerre-Gauss spectrum via projective, phase-flattening measurement, J. Opt. Soc. Am. B **31**, A20 (2014).

[51] Frédéric Bouchard, Natalia Herrera Valencia, Florian Brandt, Robert Fickler, Marcus Huber, and Mehul Malik, Measuring azimuthal and radial modes of photons, Opt. Express **26**, 31925 (2018).

[52] J. A. Arnaud, W. M. Hubbard, G. D. Mandeville, B. de la Clavière, E. A. Franke, and J. M. Franke, Technique for fast measurement of Gaussian laser beam parameters, Appl. Opt. **10**, 2775 (1971).

[53] D. V. Strekalov, A. V. Sergienko, D. N. Klyshko, and Y. H. Shih, Observation of Two-Photon "Ghost" Interference and Diffraction, Phys. Rev. Lett. **74**, 3600 (1995).

[54] T. B. Pittman, Y. H. Shih, D. V. Strekalov, and A. V. Sergienko, Optical imaging by means of two-photon quantum entanglement, Phys. Rev. A **52**, R3429 (1995).

[55] Anand Kumar Jha, Jonathan Leach, Barry Jack, Sonja Franke-Arnold, Stephen M. Barnett, Robert W. Boyd, and Miles J. Padgett, Angular Two-Photon Interference and Angular Two-Qubit States, Phys. Rev. Lett. **104**, 010501 (2010).

[56] J Just, A. Cavanna, M. V. Chekhova, and G. Leuchs, Transverse entanglement of biphotons, New J. Phys **15**, 083015 (2013).

[57] E. C. Paul, M. Hor-Meyll, P. H. Souto Ribeiro, and S. P. Walborn, Measuring spatial correlations of photon pairs by automated raster scanning with spatial light modulators, Sci. Rep. **4**, 00 (2014).

[58] Lixiang Chen, Tianlong Ma, Xiaodong Qiu, Dongkai Zhang, Wuhong Zhang, and Robert W. Boyd, Realization of the Einstein-Podolsky-Rosen Paradox using Radial Position and Radial Momentum Variables, Phys. Rev. Lett. **123**, 060403 (2019).

[59] Jessica Bavaresco, Marco Túlio Quintino, Leonardo Guerini, Thiago O Maciel, Daniel Cavalcanti, and Marcelo Terra Cunha, Most incompatible measurements for robust steering tests, Phys. Rev. A **96**, 22110 (2017).

[60] Natalia Herrera Valencia, Vatshal Srivastav, Matej Pivoluska, Marcus Huber, Nicolai Friis, Will McCutcheon, and Mehul Malik, High-dimensional pixel entanglement: Efficient generation and certification, Quantum **4**, 376 (2020).

[61] S. S. Straupe, D. P. Ivanov, A. A. Kalinkin, I. B. Bobrov, and S. P. Kulik, Angular Schmidt modes in spontaneous parametric down-conversion, Phys. Rev. A **83**, 60302 (2011).

[62] S. P. Walborn and A. H. Pimentel, Generalized Hermite-Gauss decomposition of the two-photon state produced by spontaneous parametric down conversion, J. Phys. B: At., Mol. Opt. Phys. **45**, 165502 (2012).

[63] C. K. Law and J. H. Eberly, Analysis and Interpretation of High Transverse Entanglement in Optical Parametric Down Conversion, Phys. Rev. Lett. **92**, 127903 (2004).

[64] W. P. Grice, R. S. Bennink, D. S. Goodman, and A. T. Ryan, Spatial entanglement and optimal single-mode coupling, Phys. Rev. A **83**, 023810 (2011).

[65] P. Ben Dixon, Danna Rosenberg, Veronika Stelmakh, Matthew E. Grein, Ryan S. Bennink, Eric A. Dauler, Andrew J. Kerman, Richard J. Molnar, and Franco N. C. Wong, Heralding efficiency and correlated-mode coupling of near-IR fiber-coupled photon pairs, Phys. Rev. A **90**, 043804 (2014).

[66] Daniel Ljunggren and Maria Tengner, Optimal focusing for maximal collection of entangled narrow-band photon pairs into single-mode fibers, Phys. Rev. A **72**, 062301 (2005).

[67] Sébastien Designolle, Vatshal Srivastav, Roope Uola, Natalia Herrera Valencia, Will McCutcheon, Mehul Malik, and Nicolas Brunner, Genuine High-Dimensional Quantum Steering, Phys. Rev. Lett. **126**, 200404 (2021).

[68] Natalia Herrera Valencia, Vatshal Srivastav, Saroch Leedumrongwatthanakun, Will McCutcheon, and Mehul

Malik, Entangled ripples and twists of light: Radial and azimuthal Laguerre–Gaussian mode entanglement, J. Opt. **23**, 104001 (2021).

[69] Filippo M. Miatto, Alison M. Yao, and Stephen M. Barnett, Full characterization of the quantum spiral bandwidth of entangled biphotons, Phys. Rev. A **83**, 33816 (2011).

[70] V. D. Salakhutdinov, E. R. Eliel, and W Löffler, Full-Field Quantum Correlations of Spatially Entangled Photons, Phys. Rev. Lett. **108**, 173604 (2012).

[71] Suraj Goel, Saroch Leedumrongwatthanakun, Natalia Herrera Valencia, Will McCutcheon, Claudio Conti, Pepijn W. H. Pinkse, and Mehul Malik, Inverse-design of high-dimensional quantum optical circuits in a complex medium, (2022), ArXiv:2204.00578.

[72] Timur Sh. Iskhakov, Vladyslav C. Usenko, Ulrik L. Andersen, Radim Filip, Maria V. Chekhova, and Gerd Leuchs, Heralded source of bright mesoscopic sub-Poissonian light, Opt. Lett. **41**, 2149 (2016).

[73] Sven Ramelow, Alexandra Mech, Marissa Giustina, Simon Groblacher, Witlef Wieczorek, Jörn Beyer, Adriana Lita, Brice Calkins, Thomas Gerrits, Sae Woo Nam, Anton Zeilinger, and Rupert Ursin, Highly efficient heralding of entangled single photons, Opt. Express **21**, 6707 (2013).

[74] S Castelletto, I. P. Degiovanni, and V. Schettini, Spatial and spectral mode selection of heralded single photons from pulsed parametric down-donversion, Opt. Express **13**, 6709 (2005).

[75] Mehul Malik and Robert W. Boyd, Quantum imaging technologies, Riv Nuovo Cimento **37**, 273 (2014).

[76] Marta Gilaberte Basset, Frank Setzpfandt, Fabian Steinlechner, Erik Beckert, Thomas Pertsch, and Markus Gräfe, Perspectives for applications of quantum imaging, Laser Photon. Rev. **59**, 1900097 (2019).

[77] Anand Kumar Jha, Mehul Malik, and Robert W. Boyd, Exploring Energy-Time Entanglement Using Geometric Phase, Phys. Rev. Lett. **101**, 180405 (2008).

[78] Michael Kues, Christian Reimer, Piotr Roztocki, Luis Romero Cortes, Stefania Sciara, Benjamin Wetzel, Yanbing Zhang, Alfonso Cino, Sai T Chu, Brent E Little, David J Moss, Lucia Caspani, Jose Azana, and Roberto Morandotti, On-chip generation of high-dimensional entangled quantum states and their coherent control, Nature **546**, 622 (2017).

[79] Anthony Martin, Thiago Guerreiro, Alexey Tiranov, Sébastien Designolle, Florian Fröwis, Nicolas Brunner, Marcus Huber, and Nicolas Gisin, Quantifying Photonic High-Dimensional Entanglement, Phys. Rev. Lett. **118**, 110501 (2017).

[80] Zhenshan Yang, Marco Liscidini, and J. E. Sipe, Spontaneous parametric down-conversion in waveguides: A backward Heisenberg picture approach, Phys. Rev. A **77**, 033808 (2008).